Author/s:
Abu Rowin, W;Deshpande, R;Wang, S;Kozul, M;Chung, D;Sandberg, RD;Hutchins, N

Title:
Experimental characterisation of Kelvin-Helmholtz rollers over riblet surfaces

Date:
2025-04-28

Citation:
Abu Rowin, W., Deshpande, R., Wang, S., Kozul, M., Chung, D., Sandberg, R. D. & Hutchins, N. (2025). Experimental characterisation of Kelvin-Helmholtz rollers over riblet surfaces. Journal of Fluid Mechanics, 1009, pp.a65-. https://doi.org/10.1017/jfm.2025.306.

J. Fluid Mech. (2025), vol. 1009, A65, doi:10.1017/jfm.2025.306

JFM PAPERS

Experimental characterisation of Kelvin–Helmholtz rollers over riblet surfaces

W. Abu Rowin[1], **R. Deshpande**[1], **S. Wang**[1], **M. Kozul**[1], **D. Chung**[1],
R.D. Sandberg[1] **and N. Hutchins**[1]

[1]Department of Mechanical Engineering, University of Melbourne, Melbourne, VIC 3010, Australia
Corresponding author: W. Abu Rowin, aburowin@ualberta.ca

(Received 4 November 2024; revised 14 February 2025; accepted 17 March 2025)

The formation of Kelvin–Helmholtz-like rollers (referred to as K–H rollers) over riblet surfaces has been linked to the drag-increasing behaviour seen in certain riblet geometries, such as sawtooth and blade riblets, when the riblet size reaches sufficiently large viscous scales (Endrikat *et al.* (2021*a*), *J. Fluid Mech.* **913**, A37). In this study, we focus on the sawtooth geometry of fixed physical size, and experimentally examine the response of these K–H rollers to further increases in viscous scaled riblet sizes, by adopting the conventional approach of increasing freestream speeds (and consequently, the friction Reynolds number). Rather than continual strengthening, the present study shows a gradual weakening of these K–H rollers with increasing sawtooth riblet size. This is achieved by an analysis of the roller geometric characteristics using both direct numerical simulations and hot-wire anemometry databases at matched viscous scaled riblet spacings, with the former used to develop a novel methodology for detecting these rollers via streamwise velocity signatures (e.g. as acquired by hot wires). Spectral analysis of the streamwise velocity time series, acquired within riblet grooves, reveals that the frequencies (and the streamwise wavelengths) of the K–H rollers increase with increasing riblet size. Cross-correlation spectra, estimated from unique two-point hot-wire measurements in the cross-plane, show a weakening of the K–H rollers and a reduction in their wall-normal coherence with increasing riblet size. Besides contributing to our understanding of the riblet drag-increasing mechanisms, the present findings also have implications for the heat transfer enhancing capabilities of sawtooth riblets, which have been associated previously with the formation of K–H rollers. The present study also suggests conducting future investigations by decoupling the effects of viscous scaled riblet spacing and friction Reynolds numbers, to characterise their influence on the K–H rollers independently.

Key words: drag reduction, riblets, Kelvin–Helmholtz

---

1. Introduction

The Kelvin–Helmholtz (K–H) instability can be noted in various free-shear flow phenomena of engineering importance, such as in the wake of a moving vehicle, in a turbulent jet, or in the upper layers of the atmospheric boundary layer. This instability arises from the interaction between adjacent layers of fluid(s) having a mismatch in their velocities (and densities), resulting in the formation of wave-like structures. As these instabilities develop, they can give rise to large tube-shaped formations known as K–H rollers (Drazin & Reid 2004). In the domain of wall-bounded flows, notably, similar K–H-like structures (hereafter, K–H rollers) can occur on surfaces exhibiting high wall-normal permeability, such as permeable substrates, porous walls, vegetation or rough surfaces with grooves (Finnigan 2000; Jimenez *et al.* 2001; Breugem, Boersma & Uittenbogaard 2006; García-Mayoral & Jiménez 2011*a*; Nepf 2012). Since these surfaces can favourably manipulate the drag and heat transfer characteristics of the overlying boundary layer, there is significant interest in understanding whether (and how) the K–H rollers influence these characteristics (Endrikat *et al.* 2021*a*; Rouhi *et al.* 2022). In the present study, we aim to evaluate the geometric extent of the K–H rollers formed over streamwise-aligned microgrooves (commonly referred to as 'riblets'), which are well known for reducing the turbulent skin-friction drag (Walsh & Lindemann 1984; García-Mayoral & Jiménez 2011*a*). The effectiveness of these riblets, which is typically quantified by the percentage reduction in drag compared to smooth wall conditions, has been found to be dependent on the viscous scaled riblet size as well as shape (Walsh & Weinstein 1978; Walsh & Lindemann 1984; Lee & Lee 2001; Jimenez *et al.* 2001). In terms of size, riblet drag reduction is defined based on either their spanwise tip spacing s (Jiménez 2004), or the square root of the cross-sectional area of these grooves, $l_g = \sqrt{A_g}$ (García-Mayoral & Jiménez 2011*a*,*b*).

Previous studies have demonstrated that drag reduction initially enhances with increasing values of s^+ or l_g^+, reaching a maximum of approximately 10 % at $l_g^+ \approx 10$, for a friction Reynolds number of $Re_\tau \approx 180$ (García-Mayoral & Jiménez 2011*a*,*b*). Here, the superscript '+' indicates normalisation by the friction velocity U_τ and the kinematic viscosity ν of the fluid, e.g. $s^+ = sU_\tau/\nu$ or $l_g^+ = l_g U_\tau/\nu$. However, as l_g^+ continues to increase, the riblets lose their capability to reduce drag, and instead exhibit an increase in drag (Walsh & Lindemann 1984; Bechert *et al.* 1997; Von Deyn *et al.* 2022). Several past studies have investigated the mechanisms responsible for this breakdown in their drag reduction capability (Choi, Moin & Kim 1993; Park & Wallace 1994; Suzuki & Kasagi 1994; Goldstein & Tuan 1998; García-Mayoral & Jiménez 2011*a*; Ran, Zare & Jovanović 2021; Chavarin & Luhar 2022), since unravelling its source could eventually assist with improving riblet performance. One hypothesis in the literature associates the decline in drag reduction with the emergence of elongated quasi-two-dimensional spanwise structures, namely K–H rollers, in the vicinity of the riblets (García-Mayoral & Jiménez 2011*a*,*b*). More recently, K–H rollers have also been linked to the favourable breakdown of the Reynolds analogy, wherein the enhancement in heat transfer exceeds the increase in frictional drag over blade riblets, characterised by thin ribs with parallel sides oriented in the streamwise direction (Kuwata 2022), as well as over narrow-angle triangular riblets (henceforth referred to as sawtooth riblets; Rouhi *et al.* 2022). These simulation-based investigations have revealed that K–H rollers are concentrated in the buffer layer just above the plane formed by the riblet tips, and coexist at nominal periodic streamwise spacing $\lambda_x^+ \approx 150$.

However, the exact flow physics behind how the K–H rollers increase drag is still unknown, fuelling speculation regarding their role in the breakdown of drag reduction. For instance, the skin-friction drag increases with increasing riblet size for all riblet shapes whenever $l_g^+ \gtrsim 10$, whereas the presence of K–H rollers has not been observed across all possible shapes. This was discovered recently via an extensive suite of numerical simulations by Endrikat *et al.* (2021*a*), who found that the K–H instability manifested only for blade riblets and 30° sawtooth riblets at low l_g^+ ($10 \lesssim l_g^+ \lesssim 40$), which is consistent with the riblet geometries considered in past K–H focused studies (García-Mayoral & Jiménez, 2011*b*; Kuwata 2022; Rouhi *et al.* 2022). However, other riblet geometries such as wide-angle sawtooth riblets, asymmetric triangular riblets or trapezoidal riblets did not exhibit any indications of the instability at any investigated l_g^+. These findings suggest that the relationship between the drag-increasing nature of riblets and the onset of K–H rollers is not universally applicable to all riblet geometries. Confirming the existence of a direct correlation between these two is important, since it would also have ramifications for the recently hypothesised association between the K–H rollers andthe favourable breakdown of the Reynolds analogy (Kuwata 2022; Rouhi *et al.* 2022).

Past simulations, predominantly conducted within a minimal channel configuration (García-Mayoral & Jiménez 2011*a*; Endrikat *et al.* 2021*a*, 2022; Kuwata 2022; Rouhi *et al.* 2022), have focused primarily on low values of l_g^+ ($\lesssim 40$). These l_g^+ values are inadequate to conclusively establish the existence and accurate spatial extent of K–H rollers across most of the drag-increasing regime. While performing comprehensive numerical simulations over a wide range of l_g^+ would be computationally demanding, achieving the same through experimental means is possible, constituting the central objective of the current study.

This study presents a novel experimental approach to evaluate the existence and size of the K–H rollers for varying l_g^+ of sawtooth riblets (with 30° tip angle). A novel methodology is proposed to detect K–H rollers based on their streamwise velocity signatures, thereby permitting detection of these structures via conventional hot-wire anemometry. This methodology is based on the well-established strategy of reconstructing the two-point correlations in the spectral domain (Del Alamo *et al.* 2004; Bailey *et al.* 2008; Baars, Hutchins & Marusic 2017; Deshpande *et al.* 2021), which would associate these K–H rollers with their characteristic length/time scales. The efficacy of this methodology is established here by first testing using a high-fidelity direct numerical simulations (DNS) database of a turbulent channel flow over riblets, which is shown to have K–H rollers overlying the riblet surface. The present paper is structured as follows. Section 2 introduces the numerical simulation and premise behind the novel K–H detection methodology, § 3 presents the experimental facility and measurement techniques employed, and § 4 discusses the spectral analysis to experimentally detect K–H rollers, with validation using the DNS results. Finally, the influence of varying s^+ on the strength and size of K–H rollers is discussed in § 5, while an instability analysis is presented in § 6 to comment on the variation in riblet porosity with increasing s^+. Throughout this paper, the symbols u, v and w represent the instantaneous velocity (lowercase), while U, V and W denote the mean velocities (uppercase) in the streamwise (x), spanwise (y) and wall-normal (z) directions, respectively.

2. Numerical dataset and methodology

This section outlines the set-up of DNS for a fully-developed turbulent channel flow. Simulations encompass both smooth and riblet surfaces, with a comparative analysis presented in § 2.2. For the riblet surface, two simulations are performed with the same riblet tip geometry and spacing, but different valley/groove shapes, to accommodate the limitations in fabrication of riblet surfaces (as will be discussed in § 3.2). Sections 2.3 and 2.4 focus on evaluating the presence of K–H rollers over these riblets, using time/space-averaged and instantaneous flow statistics, respectively. It should be noted that the simulations were performed in turbulent channel flow, whereas the experiments were conducted in a turbulent boundary layer facility. This decision was based on the assumption that riblet performance is comparable across different flow configurations when viscous scaled dimensions are matched, as shown in previous studies (García-Mayoral & Jiménez 2011*a*,*b*). The use of the boundary layer facility was driven by the available capabilities at the time, allowing for the fabrication and testing of riblets of adequate size. Nonetheless, the results for drag-increasing riblets, as discussed later, suggest that factors such as the Reynolds number or flow configuration may also influence riblet performance.

2.1. *Simulation set-up*

A fully-developed turbulent wall flow is simulated in a closed channel configuration using the High Performance Solver for Turbulence and Aeroacoutics Research (HiPSTAR), which is a well-established fourth-order-accurate compressible fluid dynamics code (Sandberg 2015). Here, we consider a flow Mach number $Ma = 0.2$ to simulate an incompressible turbulent flow over a smooth wall, as well as over riblet surfaces. All these simulations are performed at a matched friction Reynolds number $Re_\tau = hU_\tau/\nu \approx 590$, where h represents the half-height of the channel along its wall-normal direction, z. The flow is driven by a constant streamwise pressure gradient, which is kept fixed for all the riblet cases. The computational domain, as illustrated in figure 1(*a*), encompasses dimensions $L_x = 2\pi h$ in the streamwise direction and $L_y = \pi h$ in the spanwise direction. These domain proportions are chosen to effectively capture and resolve the majority of the flow dynamics, aligning with the approach elucidated by García-Mayoral & Jiménez (2012) concerning suitable simulation domain sizes for riblet studies. A no-slip boundary condition is enforced on the top and bottom walls, while periodic boundaries are implemented at the streamwise and spanwise extremes of the domain.

For the riblet cases, a sawtooth geometry with a 30° tip angle and spanwise tip spacing $s^+ \approx 43$ is considered with riblet height $h_s^+ = 80$ (refer to the dash-dotted red line in figure 1*b*), on both the top and bottom walls of the channel (figure 1*b*). This geometry is resolved numerically using the second-order-accurate boundary data immersion method described by Schlanderer *et al.* (2017). In the simulation of riblets, the numbers of mesh grid points in each direction are $N_x \times N_y \times N_z = 384 \times 1290 \times 793$, where z is the wall-normal direction. This configuration yields approximately 31 grid points per riblet period ($s^+ = 43$) based on the spanwise grid spacing $\Delta y^+ = 1.4$, which is detailed in table 1. These numbers of grid points per riblet period are sufficient for resolving the K–H rollers, as shown previously by the mesh convergence analysis of Endrikat *et al.* (2021*b*), amongst others. Apart from consideration of the conventional riblet geometry with sharp valleys (García-Mayoral & Jiménez 2011*a*; Endrikat *et al.* 2021*a*; Rouhi *et al.* 2022), simulations are also conducted for a riblet geometry possessing rounded valleys (RR43), with riblet height $h_r^+ = 71$ and base diameter $b_r^+ = 6.2$ (figure 1*b*). The latter is representative of the practical limitations experienced while fabricating ‘sharp’-valley riblets, with the current dimensions (b_r^+) matching exactly with those tested experimentally (discussed in § 3.2). Information regarding all simulations undertaken in this study is included in table 1.

2.2. *Mean flow properties over the rounded-valley riblets*

Figure 2 shows the mean streamwise velocity and Reynolds stress profiles over the rounded-valley riblets (RR43) and compares them against statistics over the smooth wall. Here, for purposes of brevity, we have not shown the profiles for the sharp-valley riblet case

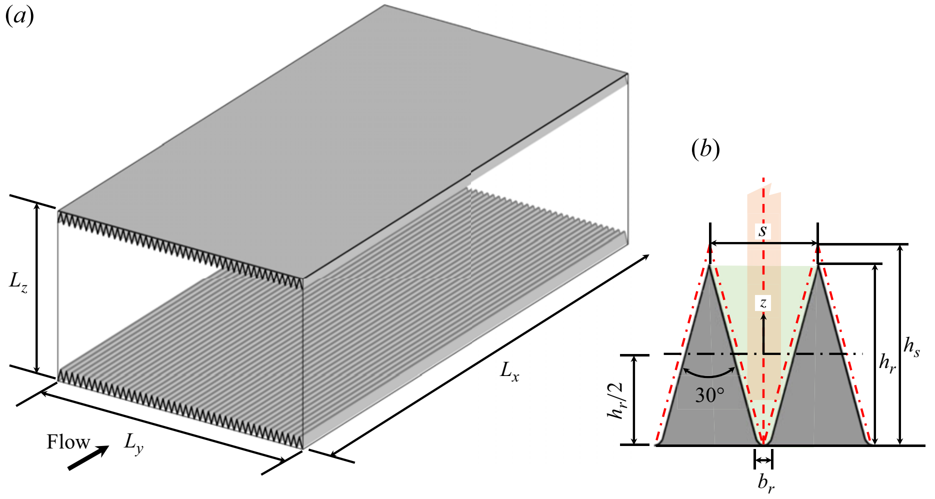

Figure 1. (*a*) DNS riblet channel domain showing the domain dimensions L_x, L_y, L_z in streamwise, spanwise and wall-normal directions, while the top and bottom walls are covered with sawtooth riblets. Here,L_z is measured from the base of the riblets. (*b*) Profile view of the rounded-valley riblet design (RR43) and the sharp-valley riblet design (SR43, shown with the dash-dotted red line) showcasing riblet characteristics such as tip spacing s, base width b_r, and height h_r or h_s, where the subscript r or s denotes the height for the rounded- or sharp-valley riblet design, respectively. The green shaded region in (*b*) corresponds to the cross-sectional area of the groove ($A_g = l_g^2$) for RR43, while the orange shaded region corresponds to the spanwise averaging region, simulating the effect of hot-wire spatial resolution on the K–H detection method discussed in § 4. The dashed vertical line in (*b*) shows the spanwise centre of the riblet grooves. Throughout this paper, we consider $z = 0$ at the riblet half-height for the corresponding riblet shape (rounded or sharp valley).

	s^+	h_r^+	h/h_r	b_r^+	l_g^+	Δx^+	Δy^+	Δz^+	L_x^+	L_y^+	Re_τ	ΔU^+
Smooth	–	–	–	–	–	9.0	4.5	0.3–6.4	3456	1728	580	–
RR43	43	71	8.3	6.2	41.3	9.7	1.4	0.3–6.4	3700	1853	590	4.1
SR43	43	80	7.3	–	41.5	9.7	1.4	0.3–6.4	3700	1853	590	4.1

Table 1. Geometry and simulation parameters for the fully-developed turbulent channel flow over a smooth wall, rounded-valley riblets (RR43) and sharp-valley riblets (SR43). The parameters include tip spacing (s^+), riblet height (h_r^+), ratio of the channel half-height to the riblet height (h/h_r), base diameter (b_r^+), square root of the groove cross-section (l_g^+), grid spacings in streamwise (Δx^+), spanwise (Δy^+) and wall-normal (Δz^+) directions, domain length (L_x^+) and width (L_y^+), the friction Reynolds number ($Re_\tau \equiv h^+ = L_z^+/2$), and the velocity roughness function (ΔU^+). Quantities denoted by a superscript '+' represent viscous scaling, i.e. non-dimensionalised using U_τ and ν.

(SR43), since they are quantitatively similar to those of the RR43 case. This similarity is expected since the change in l_g between RR43 ($l_g^+ = 41.3$) and SR43 ($l_g^+ = 41.5$) is negligible. Present findings are consistent with previous results reported by Walsh (1982, 1990) and Walsh & Lindemann (1984), who found riblet drag reduction performance to be affected on changing the riblet peak geometry but not on changing the valley curvature.

The profiles presented in figure 2 are obtained via time- and ensemble-averaging only along the spanwise centre of the riblet grooves (red dashed line in figure 1*b*). The present study considers the origin at the riblet half-height (horizontal black dash-dotted line in figure 1*b*), for analysis throughout the paper. This choice, however, does not have any substantive impact on the primary outcomes and findings of this study, which are

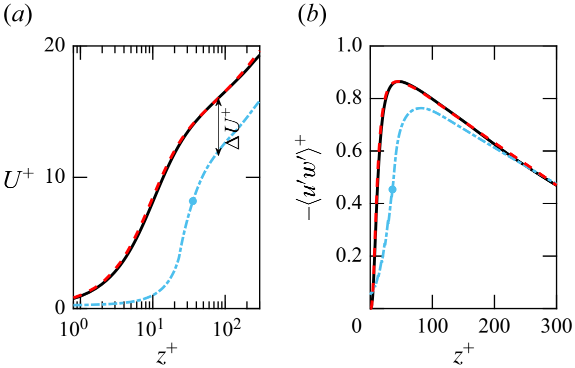

Figure 2. Viscous scaled profiles over smooth wall (black solid line) and spanwise centre of the riblet grooves (blue dash-dotted line) for (*a*) mean streamwise velocity U^+ and (*b*) Reynolds shear stress $\langle u'w'\rangle^+$, versus the viscous scaled wall-normal height. The riblet crest location, $z = h_r/2$ is shown with blue dots. The red dashed lines in (*a*) and (*b*) are from the channel DNS of Moser *et al.* (1999) at $Re_\tau = 590$. The arrow in (*a*) indicates the downward shift of the riblet velocity profile compared to the smooth wall profile, which is quantified by the velocity roughness function $\Delta U^+ = 4.1$.

associated with the detection and characterisation of K–H rollers over drag-increasing riblets. The effects of the choice of origin on drag reduction statistics are discussed in detail and represented with error bars in § 3.4.

In figure 2(*a*), the mean streamwise velocity profile over the riblet exhibits a noticeable downward shift compared to the present smooth wall profile as well as that from the simulation of Moser, Kim & Mansour (1999), at $Re_\tau = 590$. Conventionally, this shift has been associated with an increased drag penalty relative to a smooth wall. Here, we quantify this penalty via the roughness function ΔU^+, which measures the downward shift within the logarithmic region in comparison to a smooth wall profile (Clauser 1954; Hama 1954), which is approximately 4.1 for the current riblet case.

Figure 2(*b*) shows Reynolds shear stress $\langle u'w'\rangle^+$ profiles along the spanwise centre of riblet grooves. The angle brackets $\langle\,\rangle$ here denote parameters averaged in time. The effect of the current drag-increasing riblets on the Reynolds shear stress observed in figure 2(*b*) is consistent with findings of previous studies (e.g. Endrikat *et al.* 2021*a*). It is worth restating here that the Reynolds shear stress and mean velocity profiles estimated over the conventionally studied sharp-valley riblets (not presented here) are consistent with those of the rounded-valley riblets, albeit within the range of uncertainty associated with the estimation of the virtual origin. This supports our claim that the rounded valley of the current riblet geometry has negligible effect on the mean momentum field.

2.3. *Assessment of the presence of K–H rollers*

In the current study, we are simulating 30° sawtooth riblets with rounded valleys, which also have viscous scaled spacing ($s^+ \approx 43$) relatively higher than the majority of past investigations (based on sharp valleys). Hence before we can use this database to propose a new K–H detection methodology, it is necessary to investigate whether the rounded-valley shape adversely influences the presence of K–H rollers. In the literature, one of the most common methodologies/metrics adopted to confirm the presence of K–H rollers has been the analysis of the two-dimensional (2-D) spectra of u, w or the Reynolds shear stress co-spectra. For instance, García-Mayoral & Jiménez (2011*a*) analysed the 2-D energy co-spectra to show that these roller structures are concentrated in the buffer layer, just above the plane of the riblet tips, and extend across the spanwise direction.

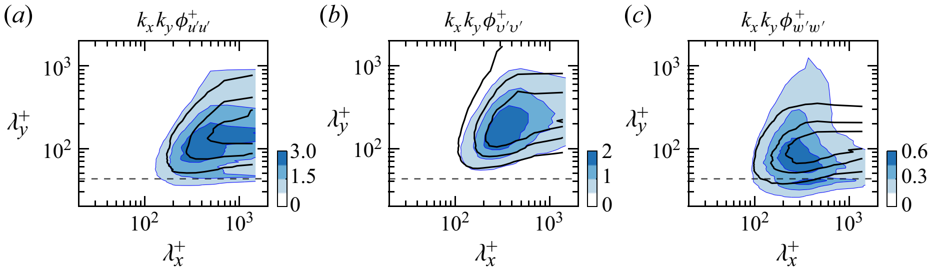

Figure 3. Two-dimensional pre-multiplied spectral energy densities of (*a*) u'^2, (*b*) v'^2 and (*c*) w'^2 for smooth surfaces (black solid contour lines) and riblet surfaces (blue shading contours encapsulated in blue contour lines). Contours for both walls are computed at $z^+ \approx 40$, which corresponds to five viscous units above the riblet crest. The horizontal dashed line is at $\lambda_y^+ = s^+$.

Their spectra indicated distinct streamwise spacing $\lambda_x^+ \approx 150$ for the K–H rollers, with the energy distributed across a wide spanwise wavelength range $\lambda_y^+ \gtrsim 300$, consistent with the existence of spanwise rollers. Similar structures were confirmed over 30° sawtooth riblets with $s^+ = 30$ by Endrikat *et al.* (2021*a*), based on the same metrics.

Inspired by these past investigations, we also compute the pre-multiplied 2-D spectral energy densities ($k_x k_y \phi^+_{u_i' u_i'}$) of all three velocity components, at a wall-normal position 5 wall units above the riblet tips. Here, k_x and k_y are the wavenumbers in the streamwise and spanwise directions. Figure 3 depicts these pre-multiplied 2-D spectra for the RR43 case, where the data from the reference smooth wall at the same wall-normal height is also included for comparison as solid black contours. Here, the energy contours of the u- and v-spectra (figure 3*a,b*) exhibit nominally similar characteristics for both the riblet and smooth wall cases. However, the w'-spectra in figure 3(*c*) reveal a distinct energy accumulation in a spectral region near $\lambda_x^+ \approx 280$, which extends for spanwise wavelengths across $100 \lesssim \lambda_y^+ \lesssim 1000$. This indicates the presence of wide structures in the spanwise direction, and relatively shorter structures in the streamwise direction, which is a distinguishing characteristic of the K–H rollers. We consider this as confirmation of the existence of K–H rollers over the present sawtooth riblets with rounded valleys (Endrikat *et al.* 2021*a*). It is also worth noting that these K–H rollers exhibit slightly higher streamwise wavelengths, $\lambda_x^+ \approx 280$, compared to those observed for blade riblets and 30° sawtooth riblets with smaller viscous scaled spacing $s^+ = 15{-}30$ ($\lambda_x^+ \approx 170$; Endrikat *et al.* 2021*a*). This suggests that the streamwise wavelength of the K–H rollers is likely dependent on the riblet shape and/or viscous scaled size, which will be investigated further in the present study. However, we noticed that the minor change of the valley between RR43 and SR43 (not shown here) did not change the streamwise wavelength of the K–H rollers.

In order to provide a clear visual representation of the presence of K–H rollers over the present riblet geometry, we employ another methodology proposed by Endrikat *et al.* (2021*a*), of plotting the instantaneous streamwise wall-shear stress on the riblet surface. Previous works have adopted a similar methodology to highlight the extension of the K–H rollers (e.g. within the grooves of riblets; Endrikat *et al.* 2021*a*), and to reveal their influence on the near-wall region, despite their origin at the crest of the riblets. Figure 4 shows the distribution of the instantaneous streamwise wall-shear stress on the present RR43 riblet surface, revealing quasi-streamwise periodic negative wall-shear stress events (i.e. reversed flow) existing simultaneously and coherently across multiple spanwise adjacent grooves. These events are representative of the spanwise coherent structures

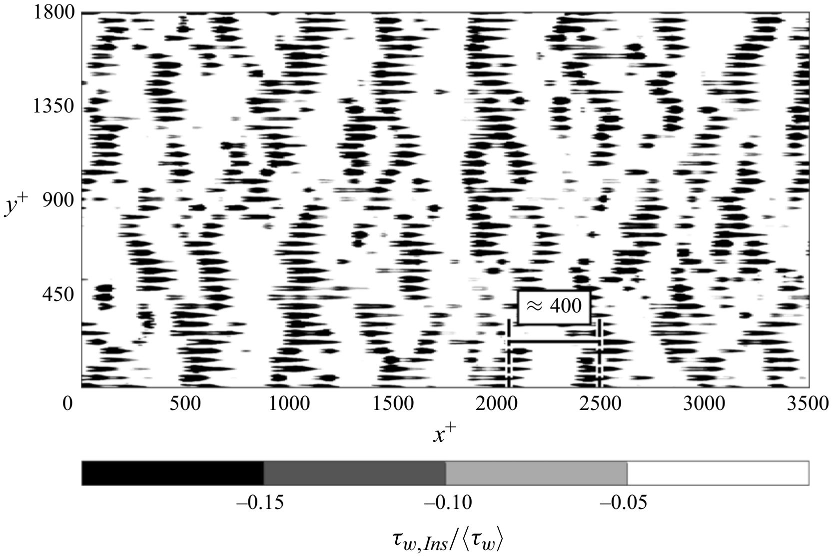

Figure 4. Instantaneous streamwise wall-shear stress ($\tau_{w,Ins}$) on the riblet surface, normalised by the average wall-shear stress ($\langle\tau_w\rangle$) on the entire surface. The vertical dashed lines indicate the streamwise distance between two negative events of the streamwise wall-shear stress to be representative of the nominal streamwise distance between subsequent K–H rollers.

(i.e. K–H-like instability) in the overlying flow, at average streamwise spacing approximately 200–400 viscous units ($\lambda_x^+ \approx 200-400$), thereby confirming the footprint of the K–H rollers below the riblet crest. The spanwise extent of these structures, however, appears to vary considerably, extending up to the spanwise size of the simulation domain L_y (≈ 1800 viscous units) in certain regions, while being limited to sizes of the order of 100 viscous units in other regions. The 'intermittent' nature of the K–H rollers is consistent with observations from previous simulations over riblets (García-Mayoral & Jiménez 2012), reaffirming the idea that these K–H rollers do not always extend across an infinite span in an instantaneous sense. The focus of this study is to explore, through experimental means, whether the spanwise extent or coherence of the K–H rollers changes with variations in the riblet tip spacing (denoted as s^+), corresponding to changes in friction drag. It is motivated by the Reynolds shear stress co-spectra analysed by Endrikat *et al.* (2021*a*) in their figure 8(*h*,*i*), in which the signature of the K–H rollers over 30° sawtooth riblets was shown to broaden spectrally (i.e. no longer narrowband at one fixed x wavelength), and also shift to a higher wavelength with increasing l_g^+. A similar observation was also noted in the modelling effort by Chavarin & Luhar (2020), where the streamwise wavelength of spanwise-constant structures (corresponding to the K–H rollers) was found to increase with riblet size. This change in the signature of the K–H rollers will be investigated here comprehensively, by conducting experiments across a significantly extended range of l_g^+ (or s^+) values.

2.4. *Near-wall signature of K–H rollers in the instantaneous streamwise velocity*

The preceding subsection establishes the presence of K–H rollers for the present DNS of rounded-valley sawtooth riblets with 30° tip angles (RR43), using methodologies adopted by past simulation studies. Employing the same methodologies for an experimental investigation, however, is challenging owing to the difficulties associated with synchronously measuring multiple velocity components in the close vicinity of the riblet crests (to obtain the Reynolds shear stresses or w^2), or measuring the wall-shear stress within the grooves. The former is possible only via conducting particle image velocimetry measurements in the streamwise/wall-normal plane close to the riblet crests, or through the use of multi-wire hot-wire anemometry, which face challenges associated with laser reflection from the wall and spatial resolution issues, respectively. These limitations can be bypassed by using conventional single-wire anemometry, which would, however, require the capability of detecting K–H rollers based solely on the streamwise velocity signatures. Here, we explore the possibility of such an approach by using the present numerical simulation as a test case.

The fact that the K–H rollers extend into the valleys and influence the streamwise wall-shear stress simultaneously across multiple adjacent grooves (figure 4) suggests that there is merit in probing simultaneously acquired, instantaneous streamwise velocity signatures across various z^+ and along the span. An example of this is depicted in figure 5, which uses the same time instant shown previously in the instantaneous streamwise wall-shear stress in figure 4. To enhance clarity, negative events (i.e. recirculation) are excluded by taking the 'absolute' value of the velocity signal, to simulate the scenario of a hot-wire measurement (which is insensitive to flow reversals), and the colour bar is chosen in a way that would reveal the near-wall low-magnitude events. After making these adjustments, the contour plot clearly reveals the presence of recurring high-fluctuation events (relative to the low mean speed near the wall) along the x direction, which are consistent with the negative wall-shear stress events observed in figure 4. These events are spaced at intervals of approximately $200 \lesssim \Delta x^+ \lesssim 400$, which closely matches the wavelength of the K–H rollers noted from spectra in figure 3. It has been verified that the same events can also be observed by simply plotting u^+, and hence are not an artefact of taking the absolute value (not shown here).

Next, to assess the spanwise extent of these extreme fluctuation events, figure 5(*b–d*) has been selected to depict $|u^+|$ in the adjacent riblet grooves in the wall-normal plane (see figure 5*a*). They indicate that the high-fluctuation events span multiple riblet spacings along the span (here, approximately three riblets, with spanwise spacing approximately 86 wall units), thus confirming their connection with the characteristic overlying K–H rollers and their manifestation on the wall (depicted in figure 4). In figure 5(*e*), we also display $|u^+|$ within an xy-plane located at the riblet mid-height. This specific location matches the lowest wall-normal height achievable by the hot-wire sensor (as outlined in § 3). Interestingly, the spanwise extension of the K–H rollers at this particular wall-normal height seems to be comparatively narrower than the extension inferred from the streamwise wall-shear stress shown in figure 4. This difference in spanwise extent is likely owing to the increased disruption of the rollers closer to the crest by enhanced turbulence/mixing activity expected in the region. This is related to increased transpiration across the riblet crest plane, which likely happens for large l_g^+ riblets (García-Mayoral & Jiménez 2011*b*).

The aforementioned findings thus make it clear that the three-dimensional (3-D) coherence of the K–H rollers can be detected/quantified based solely on streamwise velocity measurements within the grooves. To further support this, the clear signature of the rollers from the one-dimensional pre-multiplied spectra of streamwise velocity fluctuations will also be displayed in § 4 for the comparison between the simulation and experimental results. The present study quantifies the 3-D coherence of the K–H rollers by deploying multiple single normal hot-wire probes, to simultaneously acquire streamwise velocity signals from adjacent riblets along the span, or along the wall-normal direction within the same riblet groove. Cross-correlation analysis is conducted on this dataset to

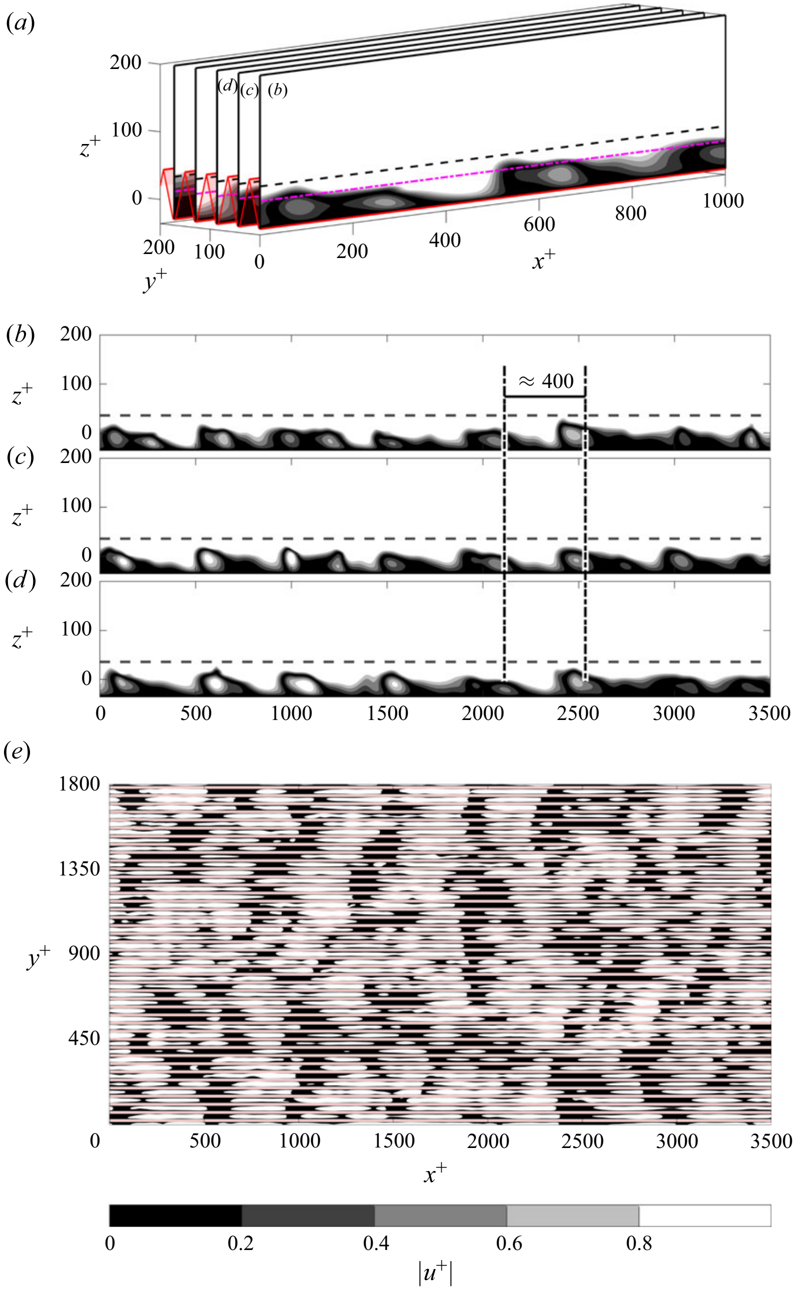

Figure 5. (*a*) Absolute value of the instantaneous streamwise velocity $|u^+|$ within multiple riblet grooves, shown up to only$(x^+ \times z^+) = (1000 \times 200)$ for clarity. (*b–d*) Samples of $|u^+|$ across the streamwise extent of the DNS domain $0 \lesssim x^+ \lesssim L_x^+$ annotated (*b*), (*c*) and (*d*) in (*a*). The dashed black line is at the riblet crest $z^+ = h_r/2$. (*e*) Plot of $|u^+|$ in an xy-plane located at the riblet mid-height, shown with a magenta dash-dotted line in (*a*). The y^+ range of (*a–d*) is in the lower part of (*e*).

investigate the spatial coherence of the K–H rollers and their sensitivity to s^+. The next section provides comprehensive details about the measurement methodology employed.

3. Experimental set-up and methodology

In this section, in § 3.1 we first describe the wind tunnel facility used in this study. Then full details about the manufactured riblets are introduced in § 3.2, including the machining process and riblet properties. Finally, the measurement techniques and validations for detecting the K–H rollers are described in §§ 3.3 and 3.4.

3.1. *Wind tunnel facility*

The experiments were conducted in an open-return boundary layer wind tunnel facility housed within the Walter Basset Aerodynamics Laboratory at the University of Melbourne. The tunnel working section has a rectangular cross-section with dimensions $0.94 \times 0.38\,\mathrm{m}^2$ in the y and z directions, respectively. The streamwise (x) length of the working section measures 6.70 m from the boundary layer trip at the inlet. All the measurements in this investigation are conducted at streamwise location $x \approx 3.80\,\mathrm{m}$ from the trip. The tunnel floor consists of eleven interchangeable main plates, each with dimensions $0.72 \times 0.50\,\mathrm{m}^2$ $(y \times x)$, as well as eight aluminium side rails. Although the tunnel floor is equipped with a heating capability, the floor temperature remained unadjusted for the specific study under consideration. Openings are present in the upper wall of the tunnel at intervals of 0.5 m in the x direction, facilitating the passage of traversing rods for hot-wire anemometer measurements. The schematics of the tunnel facility and detailed information on its characterisation can be found in Monty, Harun & Marusic (2011) and Abu Rowin *et al.* (2024).

For the present experiments, the wind tunnel is operated within a freestream velocity range $U_\infty = 5{-}20\,\mathrm{m\,s^{-1}}$. For the smooth wall case, this corresponds to a friction Reynolds number range $850 \lesssim Re_\tau \lesssim 2500$ at the measurement location. Here, the friction Reynolds number is defined as $Re_\tau = \delta U_\tau/\nu$, where δ represents the boundary layer thickness (corresponding to a height where the mean velocity U reaches 99 % of the freestream velocity U_∞), U_τ is the friction velocity obtained directly via dedicated drag balance measurements (discussed in § 3.4), and ν denotes the kinematic viscosity. It is important to highlight that our approach to varying the viscous scaled riblet spacing (s^+ or l_g^+) involves manipulating the tunnel freestream velocity, thereby influencing Re_τ. While this methodology may introduce interdependencies between changing s^+ and altering Re_τ, it remains a valid strategy for our investigation. This methodology is also consistent with previous studies, e.g. Gatti *et al.* (2020), Endrikat *et al.* (2022) and Von Deyn *et al.* (2022). Moreover, this approach mirrors real-world applications, including airflow over aircraft surfaces, where both Re_τ and s^+ naturally vary concurrently across different cruising speeds and phases of flight. In our study, we have taken measures to disentangle the impact of Re_τ on the obtained results by comparing matched cases of s^+ between experiment RR43E and simulation RR43, with distinct Re_τ values ~ 1500 for RR43E and ~ 600 for RR43. This careful approach enables us to discern and attribute observed changes to either the variation in s^+ or alterations in Re_τ.

3.2. *In-house fabrication of riblets*

The riblets employed in this investigation were fabricated with a desired sawtooth cross-section, having characteristic tip angle 30°. These riblets had peak-to-peak spacing $s = 2\,\mathrm{mm}$ and riblet depth $h_r = 3.7\,\mathrm{mm}$ (refer to figure 1*b* for definitions), which was

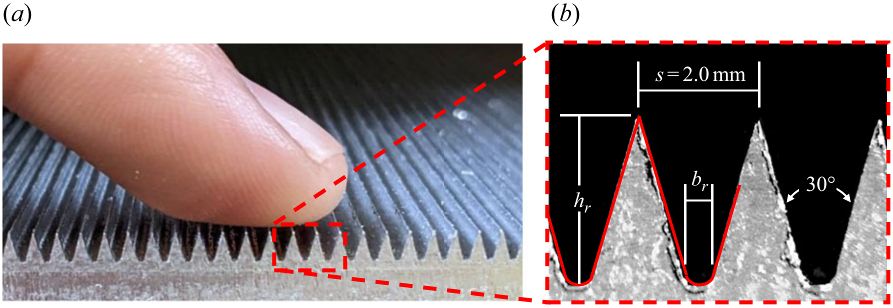

Figure 6. (*a*) A photograph depicting the overall machined riblet tile, with a finger included for scale. (*b*) A side view image showcasing the riblet details, including peak-to-peak spacing $s = 2.0$ mm, riblet depth $h_r = 3.3$ mm, tip radius $\lesssim 30\,\mu$m and base width $b_r \approx 0.3$ mm. The riblet shape is delineated by the red solid line.

designed to achieve matched s^+ and h_r^+ (with the DNS) within tunnel freestream range $7 \lesssim U_\infty \lesssim 10\,\mathrm{m\,s^{-1}}$. The riblets were manufactured in-house, within the Walter Basset Aerodynamics Laboratory, using a MultiCam three-axis CNC router. A 6061 aluminium alloy was chosen as the fabrication material in order to obtain riblets with high thermal conductivity, to be used for subsequent heated floor experiments. Obtaining deep cuts in aluminium using carbide drill bits, however, can be challenging since the drill bits are prone to wear or breakage during machining. This issue was overcome by dividing the machining task across multiple stages, which involved using multiple drill bits of varying sizes to obtain the desired riblet geometry. The final cutting procedure involved the successive passes of 2.0 mm, 1.5 mm and 1.0 mm ball nose cutters, which incrementally removed material at depths 0.70 mm, 0.75 mm and 0.73 mm, respectively. Subsequently, a 0.3 mm tapered ball nose cutter with side angle 15° was employed to eliminate an additional 1.1 mm of material. This cutting strategy required approximately five days to complete the machining process for each $720 \times 500\,\mathrm{mm}^2$ tile. The resulting shape of the machined riblet tile is presented in figure 6(*a*) as an example. For the specific tile depicted in figure 6(*b*), the dimensions of the manufactured riblets were $s = 2$ mm and $h_r = 3.3$ mm, with base width $b_r \approx 0.3$ mm. It is important to note that this rounded-valley riblet shape results in a height difference of approximately 0.4 mm compared to the ideal sharp-valley riblets, for which $h_r = 3.7$ mm. However, as mentioned in § 2.2 based on simulations of sharp- and rounded-valley riblets, the comparison of bulk properties such as ΔU^+ or the mean velocity profile revealed no discernible differences between the two cases. Consequently, the present riblet shape with rounded valleys is considered to exhibit a behaviour similar to the conventionally studied sawtooth riblets, i.e. with sharp valleys.

To ensure a fully developed turbulent boundary layer associated with the specific riblet shape under investigation, it was necessary to cover the entire floor of the wind tunnel (up to $x = 3.8$ m) with riblet surfaces, which required 11 riblet tiles in total. However, owing to constraints on time and resources, only two tiles (with combined streamwise length ~ 1 m) were manufactured using the aforementioned ‘staged machining’ procedure, to yield a riblet geometry consistent with that depicted in figure 6 (i.e. the main riblet geometry). Fabrication of the remaining nine tiles using the same staged machining procedure would have entailed approximately two more months of machining time, exceeding the available resources for this study. Consequently, a more pragmatic approach was employed, wherein 30° sawtooth riblets with base width 0.5 mm were fabricated for the remaining 9 tiles (instead of 0.3 mm base width). Independently conducted drag balance measurements revealed that such a slight modification resulted in a deviation in skin-friction drag of less than 2.5 % for the $b_r = 0.5$ mm riblets, when compared to

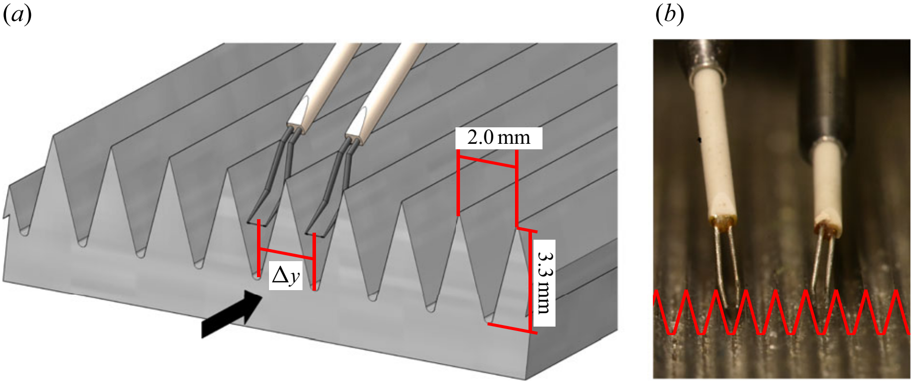

Figure 7. (*a*) Schematic of the riblets showing two hot-wire sensors deployed within the riblet grooves at spanwise separation $\Delta y = s$. (*b*) A photograph of two hot-wire sensors within the riblet grooves, for spanwise separation $\Delta y = 3s$.

the $b_r = 0.3$ mm riblets. To ensure consistent experimental conditions, the two machined tiles with base width $b_r = 0.3$ mm were placed at, and immediately upstream of, the measurement location. Such an arrangement ensured an upstream fetch of ≈ 0.8 m of the main riblet geometry, which corresponded to approximately 13 boundary layer thicknesses (13δ). By following this approach, it was expected that the boundary layer would be in a fully developed, i.e. near-equilibrium, state associated with that of the more refined ($b_r \approx 0.3$ mm) riblet geometry.

3.3. *Hot-wire anemometry and two-point measurement set-up*

Previous discussions (§ 2.4) on the near-wall footprint of the K–H rollers, in the instantaneous total streamwise velocity, have paved the way for detection of K–H rollers based on conventional hot-wire anemometry (i.e. using single-normal hot-wire sensors). The miniature design of these sensors also makes it convenient to deploy the hot-wire probes within the grooves of the riblets, having 2 mm spacing at the peak. In the present study, we deployed a modified version of a Dantec boundary layer type probe (55P15), to facilitate measurements as low as the mid-height of the present riblet geometry (i.e. $z \approx 0$; figure 7). The sensor is prepared in-house using a Wollaston wire with a Pt-core of diameter $d \approx 2.5\,\mu$m, which is exposed to a length $l \sim 0.5$ mm via etching using nitric acid. This ensures a length-to-diameter ratio (l/d) nearly equal to 200, while also keeping the spanwise extent of the sensor within 1.0 mm, which is required to access the riblet mid-height. The length of the stubs, on either side of the Pt-sensor, was approximately 0.1 mm to avoid conduction losses from the prongs while minimising the overall width of the probe.

During experiments, the hot-wire probe was operated in constant temperature mode using a custom-designed Melbourne University constant temperature anemometer at overheat ratio 1.8. Probe calibration was conducted in the freestream of the wind tunnel both before and after each velocity profile measurement, based on fifteen freestream velocities ranging from zero to 1.2 times the desired freestream velocity of the specific measurement. The resulting hot-wire voltage curves are then fitted with a third-order polynomial curve to obtain the calibration coefficients. For each boundary layer profile measurement, the hot-wire probe traversed at least 40 wall-normal locations, spaced logarithmically across $0 \lesssim z \lesssim \delta$. At each of these z locations, the hot-wire signal was acquired at sampling rate 40 kHz for duration $T = 300$ s, ensuring total acquisition time

	U_∞ (m s^{-1})	Re_τ	s^+	h_r^+	b_r^+	l_g^+	δ (mm)	h_r/δ	U_τ (m s^{-1})	10^3C_f	ΔU^+	l^+
RR27E (●)	5.0*	1048	27.7	45.8	4.2	26.6	75.6	0.041	0.208	3.46	1.9	7*
RR43E (●)	8.0*	1554	46.3	76.3	6.9	44.4	67.2	0.052	0.347	3.76	4.3	11*
RR66E (●)	12.1*	2198	68.8	113.5	10.3	66.0	63.9	0.054	0.516	3.64	5.2	17*
RR88E (●)	16.0	2895	91.5	150.9	13.7	87.8	63.3	0.054	0.686	3.68	5.8	23
RR110E (●)	19.9	3614	113.5	187.2	17.0	108.9	62.7	0.054	0.851	3.66	6.1	28

Table 2. Bulk flow and geometry properties of the rounded-valley riblet at $x = 3.8$ m obtained from velocity measurements across a freestream velocity in the range $U_\infty \approx 5{-}20\,\mathrm{m}\,s^{-1}$. The parameters include the boundary layer thickness (δ), the blockage ratio (h_r/δ), the friction velocity (U_τ), the skin fiction coefficient ($C_f \equiv 2/(U_\infty^+)^2$), and the hot-wire spanwise spatial resolution (l^+). Boundary layer profiles were also acquired over a smooth wall at matched U_∞ and $\sim l^+$ as those indicated by * in the table.

$TU_\infty/\delta \gtrsim 20\,000$. The viscous scaled sampling period, denoted as t^+, varies between 0.09 and 1.57 amongst the various measurements, and is well within the recommendations made by Hutchins *et al.* (2009).

Using constant physical dimensions of hot-wire sensors (length $l \approx 0.5$ mm and diameter $d \approx 2.5$ µm), across different Re_τ (i.e. U_∞) cases for the riblets meant that the viscous scaled length of the sensor ($l^+ = lU_\tau/\nu$) varies across $7 \lesssim l^+ \lesssim 27$ (see table 2). Although these l^+ values are in close proximity to the recommended threshold $l^+ = 20$ for minimal spatial filtering (Ligrani & Bradshaw 1987; Hutchins *et al.* 2009), some attenuation of the small-scale energy is inevitable for increasing l^+. This attenuation, however, is not expected to significantly impact the primary conclusions of this study, since the spanwise wavelengths associated with the K–H rollers are significantly larger than the spatial cut-off associated with the hot-wire resolution (refer to figure 3).The same is evident from the detailed analysis presented later in section 5. It is also important to note that the proximity of the hot-wire sensor to the metallic riblet surface, especially when the sensor is inside the groove (figure 7), means that the wire is subjected to additional heat losses. This leads to an increased output voltage from the sensor, which incorrectly corresponds to a higher local time-averaged velocity value (Khoo *et al.* 2000). Although these effects can impact the magnitude of the mean velocity measurements within the riblet grooves, they are anticipated to have minimal impact on the primary conclusions of this study, which are predominantly based on the spectral/Fourier content of the streamwise velocity fluctuations (instead of its physical magnitude). For this reason, as well as the sensor's inability to identify instantaneous flow reversals (i.e. $U < 0$), the velocity magnitudes estimated within the valley regions could not be deemed accurate. Further details on the impact of heat losses on the hot-wire measurements, in comparison with simulation results, can be found in § 3.4.

During two-point measurements (conducted independently from the boundary layer traverse experiments discussed above), two hot-wire sensors were mounted on a unique multi-axis traversing system (figure 7), to enable reconstruction of two-point correlations of the streamwise velocity fluctuations in the cross-plane, following Deshpande *et al.* (2021). The system permitted independent numerical control of the wall-normal as well as spanwise offsets between the two hot-wire sensors, thereby facilitating quantification of the 3-D spatial coherence of the K–H rollers (with the third dimension being time). Accurate wall-normal positioning of the sensors was critical for the present measurements, and was ensured with the help of a traversable stereoscopic microscope (TS-30HS), having a depth-of-field 30 µm. The wall-normal height of each sensor was measured relative to the riblet peaks by positioning the microscope above each wire, which was itself located above

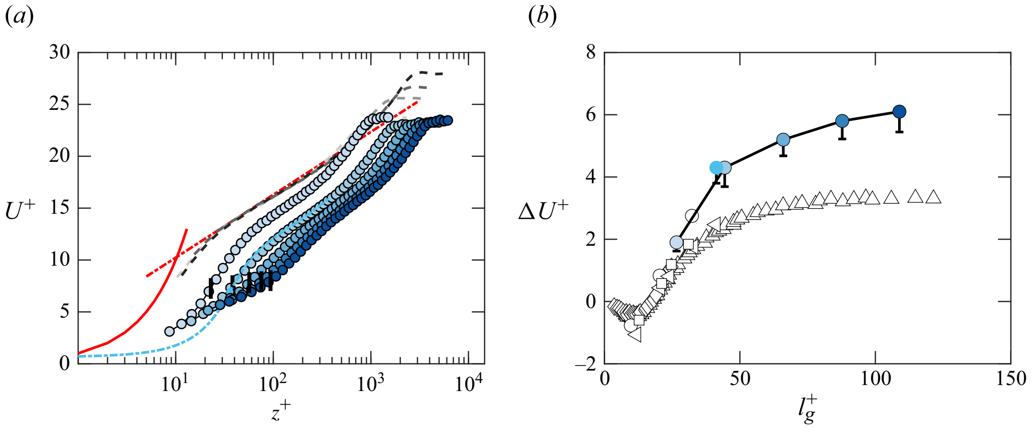

Figure 8. (*a*) Viscous scaled mean streamwise velocity U^+ as a function of the viscous scaled wall-normal distance z^+ from smooth (grey dashed lines) and riblet (filled blue circles). The crest location $z^+ = h_r^+/2$ is shown with a short vertical black line for each case. The law-of-the-wall (solid red line), log-law (red dash-dotted line) and spanwise centre of the riblet grooves (blue dash-dotted line) for the current DNS RR43 of the rounded-valley riblets are also included. (*b*) Velocity roughness function ΔU^+ of the current riblet measurement (filled blue circles) shown alongside the current DNS RR43 of the rounded-valley riblets (●), 90° triangular riblets of Bechert *et al.* (1997) (◇), trapezoidal riblets of Von Deyn *et al.* (2022) (△), and 30° sawtooth riblets (○) and blade riblets (□) of Endrikat *et al.* (2021*a*).

the crest of the riblets. The relative distance between the wire and the crest was determined with the help of a digital micrometer, which measured the distance traversed by the microscope to focus from one to another. Further, to facilitate the visual observation of the sensor as it traversed into the riblet groove, a high-resolution camera system was positioned upstream of the wire location, looking into the riblet groove. This arrangement permitted real-time monitoring of the wire as it was meticulously manoeuvred along the spanwise and wall-normal directions, to position within the riblet groove. It is worth noting here that this process of positioning the wire within the riblet groove can be subject to various sources of errors, which include uncertainties originating from the microscope system (with precision $30\,\mu\mathrm{m}$) and the transverse encoder resolution (with precision $5\,\mu\mathrm{m}$). The net uncertainty associated with initial positioning of the wire was estimated to be $\sim 30\,\mu\mathrm{m}$ (corresponding to within 1.8 viscous units). See Abu Rowin *et al.* (2024) for more details on the uncertainty analysis. Apart from the uncertainty in hot-wire positioning during wind-off conditions, a small downward movement in the wire position was also noted when the air flow was turned on. This can be attributed to aerodynamic forces that occur in any conventional hot-wire experiment, to a certain extent. It is possible that this shift becomes more pronounced at higher flow velocities.

3.4. *Validation of the mean statistics from experiments*

The mean velocity profiles for smooth and riblet cases are depicted in figure 8(*a*). Here, $U^+ = U/U_\tau$ represents the mean viscous scaled streamwise velocity, and $z^+ = zU_\tau/\nu$ denotes the viscous scaled wall-normal distance. The freestream velocity is varied within the range $U_\infty = 8{-}20\ \mathrm{m\,s^{-1}}$. The measurement over the smooth wall (shown with dashed grey shaded lines) is also performed for comparison purposes. To determine the friction velocity (U_τ) for both smooth and riblet cases, we utilised an in-house drag balance, as deployed in previous studies on trapezoidal riblets (Endrikat *et al.* 2022) and rough walls (Ramani *et al.* 2024). Details and schematics of the drag balance can be found in

Ramani *et al.* (2024). A summary of the primary flow and riblet parameters at each U_∞ condition, including U_τ, is provided in table 2. As expected for the smooth wall data in figure 8(*a*), regardless of the Re_τ (i.e. U_∞) values, all the velocity profiles overlap in the inner ($U^+ = z^+$) and logarithmic ($U^+_{log} = \kappa^{-1}\log(z^+) + A$) regions. In this context, $\kappa = 0.384$ and $A = 4.17$ represent the logarithmic constants.

Riblets have been shown previously to alter the slope in the logarithmic region (κ) (Endrikat *et al.* 2022). Thus forcing the current mean velocity profiles to match the smooth wall κ slope by altering the virtual origin was deemed unreliable. Consequently, the wall-normal origin for all riblet U^+ profiles in figure 8(*a*) is assumed to be at the riblet mid-height ($h_r/2$). The hot-wire measured profile U^+ (RR43E ●) aligns well with the current simulation RR43 (- · -), except within the valley, where the hot-wire signal overestimates U^+ due to heat losses to the wall. This overestimation affects the accuracy of the measured velocity magnitude, making it difficult to directly determine the inflection point from the velocity profile, which is often indicative of instability in shear flows (Rayleigh 1880). The measured U^+ profiles over the riblet surfaces are shifted downwards compared to that of the smooth wall. This downward shift, namely the Hama roughness function ΔU^+, is shown in figure 8(*b*). Owing to unavailability of the correct virtual origin for the current riblet study, we vary the origin between the riblet mid-height and crest. Such variations of the virtual origin lead to changes in ΔU^+, which are presented by error bars in figure 8(*b*). It is worth nothing here that the uncertainties about the exact virtual origin for each riblet case do not affect the discussion regarding K–H rollers, as all the following results related to the K–H rollers characteristic are primarily reported with reference to the riblet mid-height. Results of the current DNS RR43 of the rounded-valley riblets (●), 90° triangular riblets of Bechert *et al.* (1997) (⋄), trapezoidal riblets of Von Deyn *et al.* (2022) (△), and 30° sawtooth riblets (○) and blade riblets (□) of Endrikat *et al.* (2021*a*) are also included. For the current data, ΔU^+ appears to gradually increase with l_g^+, implying increased drag compared to the smooth wall. The small discrepancy between the experimentally estimated ΔU^+ (for $l_g^+ \approx 44$) and that of the simulations (with $l_g^+ \approx 42$) could be attributed to the different flow geometry (boundary layer for the experiments and channel for the simulation), the mismatched h_r/δ, the valley rounding and/or the measurement uncertainty, e.g. hot-wire positioning and drag balance uncertainty.

4. Spectral signature of K–H rollers in the streamwise velocity

With the experimentally acquired mean streamwise velocity statistics now established, the K–H roller characteristics are corroborated by a comparison of the energy spectra of streamwise fluctuations between simulations (RR43) and experiments (RR43E). In this context, figure 9(*a*) displays the pre-multiplied one-dimensional streamwise spectrogram of u'^+ (henceforth referred to as $k_x\phi^+_{u'u'}$), derived from DNS of channel flow over both a smooth wall and rounded-valley riblets (RR43). For the case of the DNS spectra, the spectra are averaged across multiple planes to achieve convergence. The spectrograms are presented as functions of the viscous scaled streamwise wavelength λ_x^+, and z^+ (with $z = 0$ positioned at the mid-height of the riblet). To ensure direct comparability with the experimental (hot-wire) data, $k_x\phi^+_{u'u'}$ has been computed for the DNS by considering the absolute value of the instantaneous streamwise signal, e.g. $u'^+ = |u^+| - U^+$. This procedure is similar to that applied previously to the DNS data in the discussion of figure 5; the u'^+ here is also estimated after spatially averaging the DNS data across ≈ 11 wall units in the spanwise direction, aligning with the hot-wire spatial resolution of the corresponding RR43E case ($l^+ \sim 11$; see table 2). It has been verified that the K–H rollers'

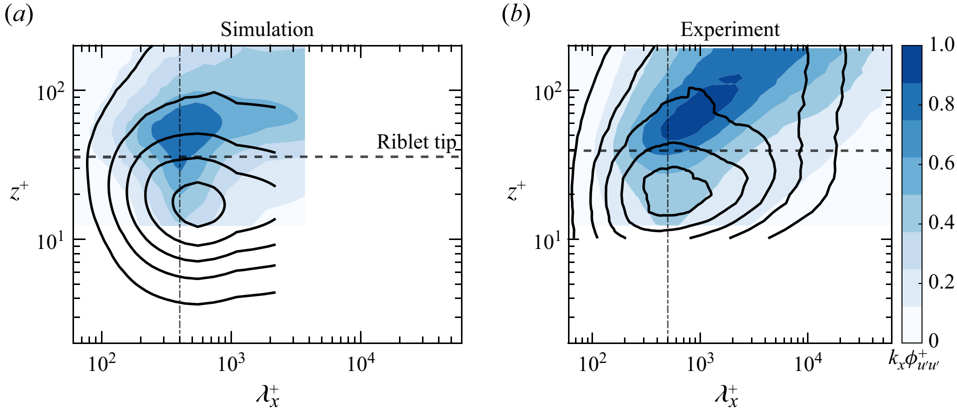

Figure 9. The one-dimensional pre-multiplied spectra of streamwise velocity fluctuations at different wall-normal positions for (*a*) simulation and (*b*) experiment results at matched viscous scaled riblet sizes. The blue contours represent the riblet data of RR43 in (*a*) and RR43E in (*b*), while the black lines represent the smooth data. The horizontal dashed lines indicate the location of the riblet crest, while vertical dash-dotted lines are at $\lambda_x^+ = 400$ in (*a*) and $\lambda_x^+ = 500$ in (*b*). These lines mark the peak of the spectra below the crest, and are assumed to represent the streamwise wavelength of the K–H rollers.

streamwise wavelength is unaffected by the spatial filtering of the DNS data (at least up to $l^+ \sim 28$ considered in this study), suggesting that variations in l^+ across the different cases would have an insignificant effect on the observed K–H roller characteristics. In the case of the experimental spectra, we average the signal over sufficiently long hot-wire signal lengths (i.e. advection length $\gtrsim 20\delta$), to achieve satisfactory convergence of the largest scales. Notably, a distinct narrowband frequency structure is observed below the riblet crest ($z^+ \lesssim h_r/2$) in the RR43 spectra, prominently at $\lambda_x^+ \approx 400$. This spectral feature near the wall contrasts with that seen on a smooth wall, occurring at $\lambda_x^+ \sim 1000$, which is associated with the classical viscous near-wall cycle (Kline *et al.* 1967; García-Mayoral & Jiménez 2011*a*). The streamwise wavelength $\lambda_x^+ \approx 400$ closely aligns with the streamwise periodicity of the K–H rollers observed earlier in figure 5, reaffirming that it represents their spectral signature. It has been checked that this spectral signature is not an artefact of estimating u'^+ based on the absolute value of the instantaneous streamwise signal, i.e. $u'^+ = |u^+| - U^+$.

Figure 9(*b*) compares the pre-multiplied spectra of u'^+ acquired by a hot-wire sensor over the RR43E riblets, with that obtained over a smooth wall, for a tunnel freestream velocity approximately $U_\infty = 8.0\,\mathrm{m\,s^{-1}}$. For converting the original frequency spectra as a function of λ_x^+ for comparison with spectra from the DNS, a constant convection velocity approximately $6U_\tau$ was employed for all u'^+ signals acquired below the riblet crest ($z^+ \leq h_r^+/2$). This choice is inspired from the past analysis of García-Mayoral & Jiménez (2011*b*) and Endrikat *et al.* (2021*a*), in which K–H rollers convect along x at $\sim 6U_\tau$. For signals above the riblet crest, Taylor's hypothesis, i.e. convection at the local mean velocity $U^+(z^+)$, was adopted. It is important to note that convection velocity approximately $6U_\tau$ is typically valid only for wide streaks (Jiménez 2018). This condition, as will be demonstrated later, applies to the K–H rollers in the current s^+ case. The experimental spectra from the RR43E case exhibit a distinct energy distribution at $\lambda_x^+ \approx 500$, in agreement with that observed from the DNS data (figure 9*a*). This observation reaffirms the existence of the K–H rollers in case of RR43E, while also demonstrating consistency with its equivalent numerical case, RR43. A noteworthy difference between

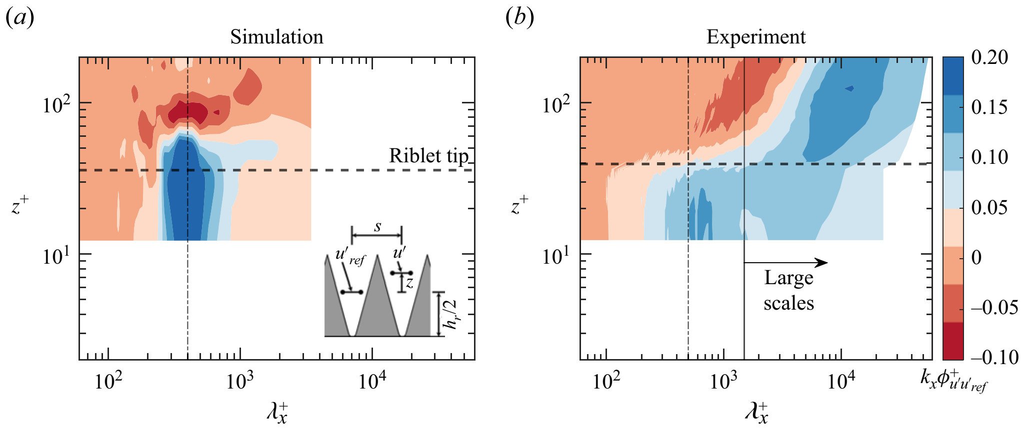

Figure 10. The co-spectra of streamwise velocity fluctuations $k_x\phi^+_{u'u'_{ref}}$ of a fixed signal located at the riblet mid-height 'reference' (denoted by 'ref') and other wall-normal traversing signal in the adjacent riblet, as shown in the schematic in the inset in (*a*), for (*a*) simulation RR43 and (*b*) experiment RR43E results at matched viscous scaled riblet sizes. The horizontal dashed lines indicate the location of the riblet crest, while vertical dash-dotted lines are at $\lambda_x^+ = 400$ in (*a*) and $\lambda_x^+ = 500$ in (*b*). These lines mark the peak of the spectra below the crest, and are assumed to represent the streamwise wavelength of the K–H rollers. The solid black vertical line in (*b*) indicates the onset of large scales at $\lambda_x^+ \approx 10^3$.

the experimental and DNS spectra in figure 9, however, is the presence of energetic large-scale inertia-dominated structures in the former ($\lambda_x^+ \gtrsim 10^4$ in figure 9*b*). We speculate that this difference can be attributed to the significantly higher Re_τ for the RR43E case, at which these structures are well-known to be statistically significant (Hutchins & Marusic 2007; Deshpande *et al.* 2021). We can therefore conclude that K–H rollers exist in the case of the RR43E riblet, which has matched viscous scaled riblet geometry to the simulated RR43 case, but with higher Re_τ.

With the spectral signature of the K–H rollers now identified, next we extend this analysis to investigate the spatial coherence (i.e. size) of these structures in the spanwise and wall-normal directions (evident from figure 5). This can be made possible by cross-correlating two synchronously acquired u'^+ signals acquired at a spatial offset (Deshpande *et al.* 2021), the spectral equivalent of which should reveal the coherence/strength of the K–H rollers at the identified $\lambda_x^+ \sim 400{-}500$. To test this idea, we compute the pre-multiplied one-dimensional cross-correlation spectra $k_x\phi^+_{u'u'_{ref}}$ (henceforth referred to as the cross-spectra) based on u'^+ signals acquired simultaneously at a spanwise offset of one riblet spacing, i.e. $\Delta y = s$ (depicted schematically in figure 7*a*). Here, the subscript 'ref' denotes the reference u'^+ signal acquired by a fixed hot-wire sensor at the mid-height of the riblet (z_{ref}), which is cross-correlated with the u'^+ signal synchronously acquired by another hot-wire sensor traversing various z^+ (but maintaining a fixed $\Delta y = s$), yielding a complex-valued $k_x\phi^+_{u'u'_{ref}}$, by definition. However, here we consider only the 'real' part of the co-spectra $k_x\phi^+_{u'u'_{ref}}$ to analyse positive and negative regions that correspond to the respective correlations (refer to Deshpande *et al.* (2021) for further clarifications and data interpretations).

Figure 10(*a*,*b*) respectively plot $k_x\phi^+_{u'u'_{ref}}$ based on the numerical (RR43) and hot-wire (RR43E) data over riblets, for the same $\Delta y^+ = s^+ \approx 43$. In figure 10(*a*), a clear positive correlation is observed between the two signals below the riblet crest, at $\lambda_x^+ \approx 400$, which is consistent with the streamwise periodicity of the K–H rollers noted previously in figure 9(*a*). This finding supports the notion that the average spatial coherence of the K–H rollers extends across a spanwise distance of at least s^+ (i.e. $\Delta y = s$). Additionally, it is not surprising to observe this positive correlation extending up to 20 viscous units above the riblet crests, given that K–H rollers are known to form above the riblet peaks, with their streamwise signature extending across tens of viscous units above these peaks (García-Mayoral & Jiménez 2012). The experimental results for RR43E in figure 10(*b*) demonstrate a trend similar to that observed for the simulations (RR43). The u'^+ signals across one riblet spacing seem positively correlated below the riblet crest at $\lambda_x^+ \approx 500$, but this correlation diminishes rapidly above it. This disparity between the experimental and DNS results, in regard to the wall-normal extension of the K–H rollers, could be attributed to the presence of an increased hierarchy of turbulent scales over the riblet crest for the high Re_τ case (Hutchins & Marusic 2007; Deshpande *et al.* 2021). This is clearly evident from the strong negative and positive correlations noted above the riblet crests in figure 10(*b*), at $\lambda_x^+ \approx 2000$ and 10^4, respectively. These respectively correspond to the wall-coherent low- and high-momentum inertial motions coexisiting in a high Re_τ boundary layer (Deshpande *et al.* 2021), which, however, are much weaker at the lower Re_τ corresponding to the simulations (figure 10*a*). To summarise, figures 9 and 10 have established the methodology to detect spectral signatures of the K–H rollers and also quantify their spatial coherence. These methodologies are employed in the next section to investigate the variation in K–H properties as a function of increasing s^+, corresponding to the drag-increasing regime of the riblets.

5. Effect of riblet tip spacing on the K–H rollers

5.1. *Variation in spectral signature of K–H rollers*

Before we investigate the variation in spatial coherence of the K–H rollers as a function of l_g^+, it is important to identify the variation (if any) in the auto-spectral signatures. For this, we begin by analysing $f\phi^+_{u'u'}$ plotted in figure 11, which is estimated from hot-wire data acquired over riblets at various s^+: $27 \lesssim s^+ \lesssim 110$ and $1000 \lesssim Re_\tau \lesssim 3500$ (refer to table 2). Here, considering that all the spectra are obtained from u'^+ time series, we have opted to plot them as functions of the viscous scaled time/frequency scales, i.e. $T^+ = U_\tau^2/f\nu$, instead of applying Taylor's hypothesis (where f indicates frequency). Consistent with figure 9, a distinct spectral signature of the K–H rollers is evident at small time scales ($T^+ \lesssim 200$) for z^+ below the riblet crest, irrespective of the variation in s^+. Their spectral signature has been marked by black rectangles in figure 11, which clearly reflect a shift in the characteristic viscous scaled time scale of the K–H rollers with increasing s^+. Potentially, this can also be interpreted as an increase in the streamwise periodic offset between the K–H rollers, with increasing s^+. It is worth noting that due to the absence of an estimate of the convection velocity at different tested l_g^+ cases, one could argue that the observed increase in the K–H wavelength might be linked to an increase in the convection velocity. Therefore, in future analyses, investigating the convection velocity could provide further insights into this issue. Another noteworthy observation from figure 11 is the reduction in spectral energy associated with the K–H rollers, with increasing s^+. This could be associated with the penetration of large-scale structures ($T^+ \gtrsim 500$) into the riblet valleys with increasing s^+, which is indicated by the relative darkening and broadening of the energy contours below the dashed line.

To better demonstrate the effect of s^+ on the existence of K–H rollers and the penetration of large scales into the groove, figure 12(*a*) showcases $f\phi^+_{u'u'}$ at the mid-height of the

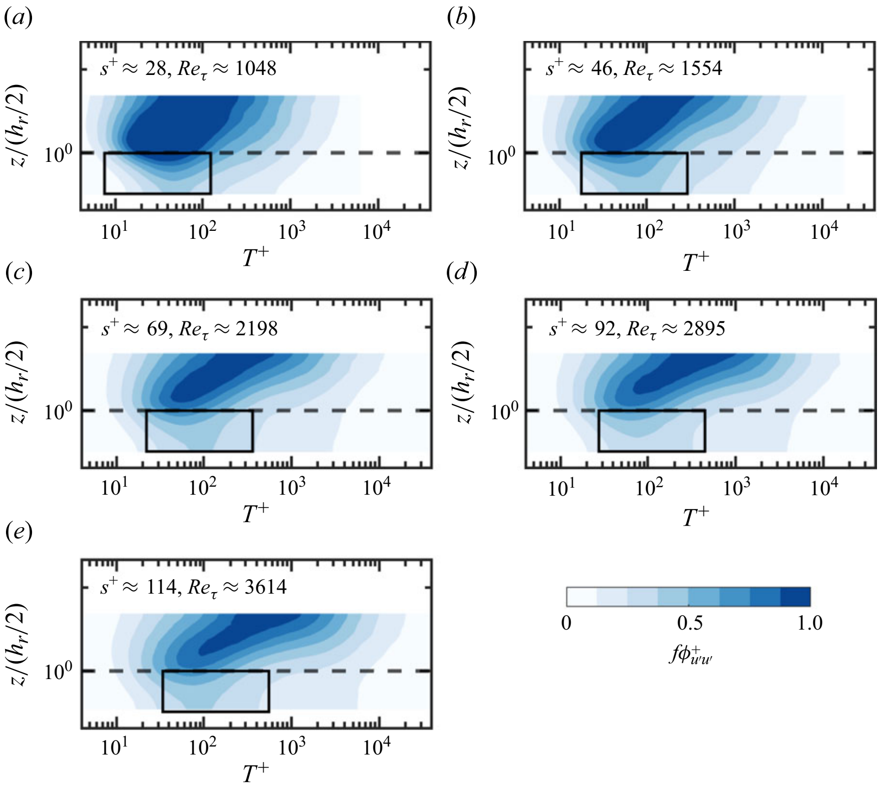

Figure 11. The viscous scaled one-dimensional pre-multiplied spectra of streamwise velocity fluctuations, denoted as $f\phi^+_{u'u'}$, obtained from experimental data. The spectra are plotted as functions of the viscous scaled time scale T^+ and the wall-normal distance normalised by half the riblet height, represented by $z/(h_r/2)$. (*a–e*) Plots corresponding to different values of tip spacing, ranging from $s^+ \approx 27$ to $s^+ \approx 110$. The horizontal dashed lines indicate the location of the riblet crest ($z/(h_r/2) = 1$). The rectangles highlight the narrowband frequency observed below the riblet crest, which serves as an indication of the presence of K–H rollers.

riblet ($z/(h_r/2) \approx 1$) for various s^+ cases plotted against T^+. The red marker × indicates that the peak of $f\phi^+_{u'u'}$ (which is representative of the K–H rollers) is most energetic for the lowest s^+ value tested (approximately 27). However, as the riblet tip spacing (s^+) increases, this peak generally undergoes attenuation and shifts towards higher T^+ values. The attenuation is not monotonic: the peak $f\phi^+_{u'u'}$ of the $s^+ = 110$ case is higher than peaks of $s^+ = 66, 88$. This trend could potentially be attributed to the downward displacement of the wire at higher flow speeds, as discussed in § 3.3. Figure 12(*b*) depicts the variation in spectral signature (T^+) of the K–H rollers (referred to as T^+_{KH}) against s^+, which demonstrates a quasi-linear relationship between these two variables for $s^+ \lesssim 110$. These observations reaffirm that the frequency of occurrence of K–H rollers is influenced by the riblet tip spacing (s^+) and/or Re_τ.

In this context, it is relevant to highlight the study by Ho & Huerre (1984), who characterised the frequency of K–H rollers by estimating the Strouhal number, defined as $St = \theta/(T_{KH}U_{KH})$. Here, U_{KH} denotes the convection velocity of the rollers, while θ represents the momentum thickness of the mixing layer associated with K–H instability. Ho & Huerre (1984) determined a Strouhal number $St \approx 0.032$ for K–H instability, a result later validated by Ghisalberti & Nepf (2002). In the present study, Strouhal numbers

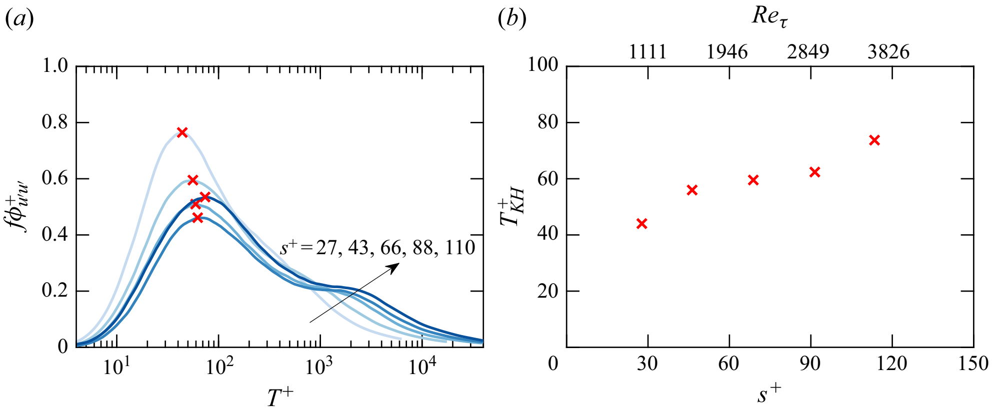

Figure 12. (*a*) The viscous scaled one-dimensional pre-multiplied spectra of streamwise velocity fluctuations $f\phi^+_{u'u'}$ at the riblet mid-height versus T^+. The darker blue shading illustrates greater s^+. The red '×' marks indicate the peaks of $f\phi^+_{u'u'}$ for K–H rollers at T^+_{KH}. (*b*) Plot of T^+_{KH} as a function of s^+. The secondary x-axis in (*b*) shows the corresponding Re_τ values; it is not linear.

were observed within the range 0.023–0.034 across the tested values of s^+, assuming $U_{KH} \approx U_{crest} \approx 6U_\tau$ (figure 8*a*) and $\theta \approx (1/4)\delta_w \approx (1/4)z_{KH}$, where δ_w is the vorticity thickness characterising the vertical extent z_{KH} of the roller structures, later measured to be 1.5 to $0.5h_r/2$ (see figure 14*b*). These observed values align closely with those reported by Ho & Huerre (1984) and Ghisalberti & Nepf (2002), further supporting the identification of the present structures as K–H rollers.

5.2. *Variation in spatial coherence of K–H rollers*

Here, we employ the cross-spectral analysis demonstrated previously in figure 10, to characterise the spatial (i.e. spanwise and wall-normal) extent of the K–H rollers. Figure 13 shows the cross-spectra of the streamwise velocity fluctuations computed between the u'^+ signal from a fixed 'reference' sensor (positioned approximately at the mid-height of a riblet groove), and the u'^+ signal from a wall-normal traversing probe, for all s^+ cases tested. To examine the spanwise coherence of the rollers, the spanwise offset between the two sensors (Δy) is varied across $0 \lesssim \Delta y/s \lesssim 5$. For the case $\Delta y = 0$, both sensors are situated within the same riblet groove, with the fixed sensor located at the riblet mid-height while the other sensor traverses vertically away from the fixed wire, starting from a minimum wall-normal separation of approximately 0.4 mm. The plots in figure 13 are arranged from left to right to reflect the increasing values of $27 \lesssim s^+ \lesssim 110$, while the vertical arrangement from top to bottom represents the ascending values of $0 \lesssim \Delta y/s \lesssim 5$. Here, since our primary focus lies on the K–H rollers, the cross-spectra are limited to $T^+ \lesssim 300$, for clarity and relevance. To isolate the effect of Re_τ of the K–H rollers, we also included the results from the simulation of RR43 in figure 13(*c*), next to the matched s^+ from the experiment over RR43E in figure 13(*b*).

In agreement with the observations made in figure 11, the plots in figure 13(*a*I–*e*I) at $\Delta y/s = 0$ reveal a positive correlation below the riblet crest, i.e. $f\phi^+_{u'u'_{ref}} > 0$, at T^+ associated with the K–H rollers (indicated by rectangles). Consistent with figure 12, the peak of this correlation shifts to higher T^+ values as s^+ increases, while the strength of the positive correlation appears to diminish with increasing s^+. Further to that, the wall-normal extent of this positive correlation, which represents the wall-normal coherence of the K–H rollers, initially extends above the riblet tips for $s^+ \approx 27$, but decreases in

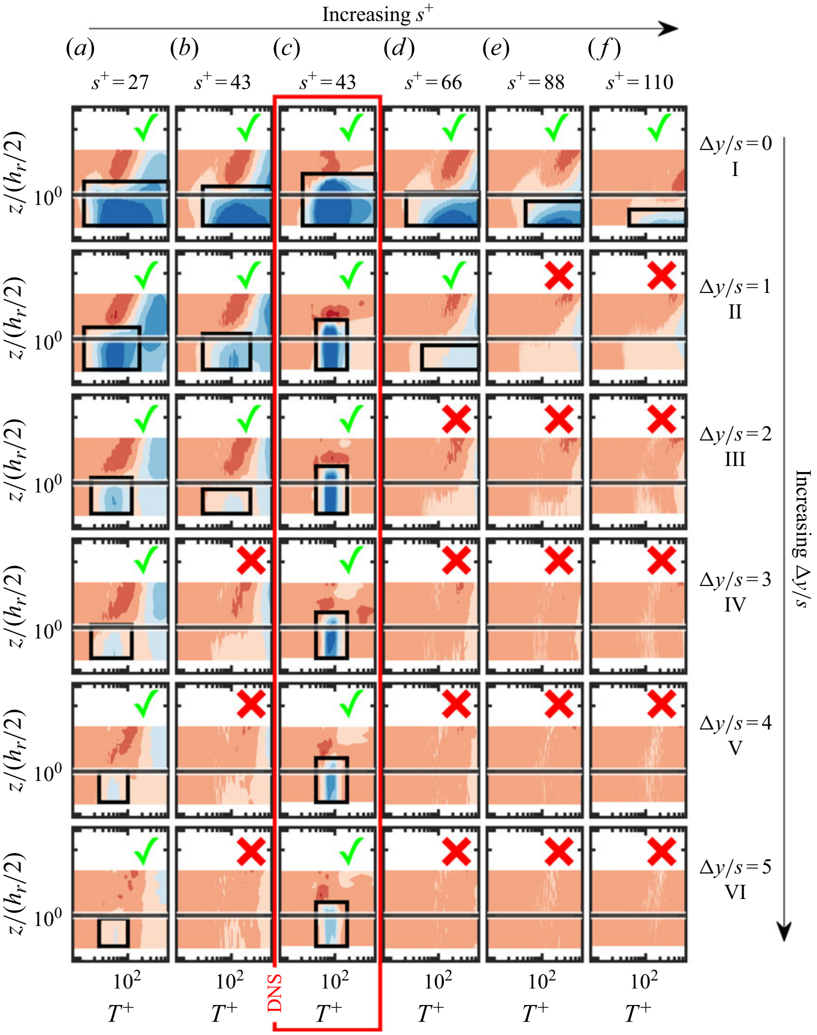

Figure 13. The viscous scaled co-spectra of streamwise velocity fluctuations $f\phi^+_{u'u'_{ref}}$ of a fixed signal located at approximately the riblet mid-height and other wall-normal traversing signals for (*a–f*) $27 \lesssim s^+ \lesssim 110$ and (I–VI) $0 \lesssim \Delta y/s \lesssim 5$. Plots in (*c*), as highlighted with a red box, are results obtained from the DNS for RR43, with the exact configuration (z and y locations, spatial resolution and absolute value of the signal) of the experiments of the other columns. The horizontal solid lines indicate the location of the riblet crest at $z/(h_r/2)=1$. The rectangles highlight the positive correlation below the crest as indication of K–H rollers. The greentick and redcross symbols refer to detected and undetected K–H rollers, respectively.

height until it is confined near the mid-height of the riblet, at $s^+ \approx 110$. Hence the first row of plots in figure 13 suggest that the wall-normal coherence as well as the strength of the K–H rollers decreases as s^+ increases. Next, to investigate the cross-spectra for various spanwise separations, we just view the columns of co-spectra in figure 13 for each viscous scaled riblet size s^+. For the smallest riblet size ($s^+=27$, in figure 13*a*I–*a*VI) the distinct signature of the K–H rollers is evident for all spanwise separations ($\Delta y/s \lesssim 5$). For larger $s^+ \gtrsim 43$ cases of the experimental results, however, coherence of these K–H rollers appears to decrease as $\Delta y/s$ increases.

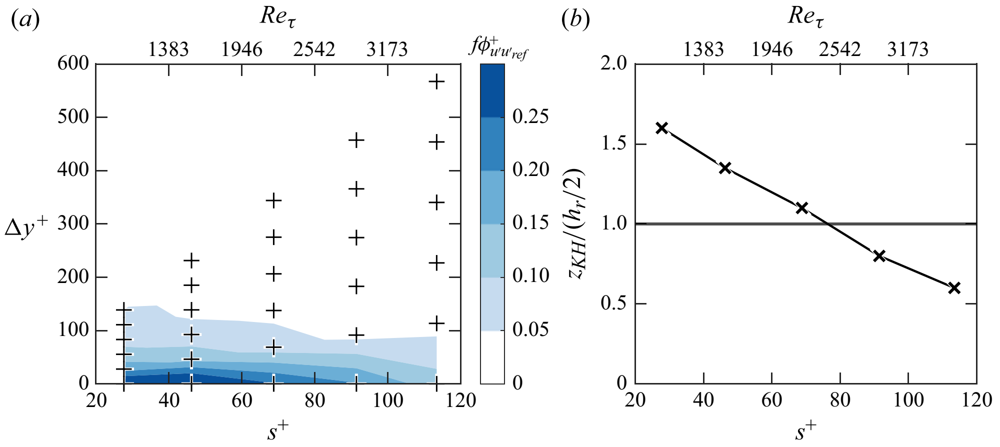

Figure 14. (*a*) Contours of the peaks of $\phi^+_{u'u'_{ref}}$ at T_{KH} below the crest as a function of the two wires viscous scaled spanwise separation Δy^+ and s^+. The $+$ marks show the measurement points, while the rest of the contour is interpolated. (*b*) The variation in wall-normal coherence ($z_{KH}/(h_r/2)$) as a function of s^+, shown with the $\times$ marks. The secondary x-axis in (*a*) and (*b*) shows the corresponding Re_τ values; it is not linear.

The influence of Re_τ on the characteristics of K–H rollers becomes evident upon comparing figure 13(*b*) for RR43E at $Re_\tau \approx 1500$ and figure 13(*c*) for RR43 at $Re_\tau \approx 600$. Examining the first row of figure 13(*b*,*c*) at $\Delta y/s = 0$, the coherence of K–H rollers is notably narrower in band $50 \lesssim T^+ \lesssim 300$ for RR43 in comparison to the range $T^+ \gtrsim 50$ for RR43E. This distinction is largely attributed to the deeper penetration of large-scale structures into the riblet valleys, influenced by the substantially higher Re_τ in the case of RR43E, aligning with the observations of figure 11. Of particular interest is the discernible interruption in the spanwise extension of K–H rollers induced by the elevated Re_τ in the RR43E case (see figure 13(*b*,*c*)I–VI). The coherence of K–H rollers experiences a loss at $\Delta y/s \approx 4$ for RR43E, whereas it remains comparatively robust until $\Delta y/s \approx 5$ for the RR43 case. These findings collectively underscore the substantial influence of increasing Re_τ in disturbing the K–H rollers. We should also note that between the current simulation (RR43) and experimental (RR43E) cases, the ratios of the riblet height to the boundary layer thickness are substantially different, and could also contribute to the differences observed between the two cases.

Overall, figure 13 suggests that both the spanwise and wall-normal extents of the K–H rollers are influenced by s^+ or Re_τ. Notably, for large $s^+ \approx 110$, the spatial coherence of the K–H rollers is confined to a single valley, indicating a deviation from their typical ‘spatial extension’ along the span. To analyse the spanwise extension of the rollers in viscous scaling (i.e. Δy^+), instead of $\Delta y/s$ as done in figure 13, we plot in figure 14(*a*) contours of the peak of $f\phi_{u'u'_{ref}}$ (i.e. at T^+_{KH}) at $z^+ \lesssim h^+_r/2$, as a function of Δy^+ and s^+. Since in this study s^+ is varied simultaneously with Re_τ, the corresponding Re_τ values for each case are shown on the top axes of figure 14. This highlights the coupled variation and underscores the limitation in isolating the individual effects of s^+ and Re_τ within the present dataset. The strength of the K–H rollers appears to slightly reduce as s^+ increases. This, however, should not be confused with the spanwise extent of the near-wall cycle, given that it has a distinctly different $T^+ \sim 100$ than noted for T^+_{KH} in figure 12(*a*). Figure 14(*b*) additionally presents the wall-normal extension of K–H rollers, denoted as $z_{KH}/(h_r/2)$ plotted against s^+ for values acquired from the first row ($\Delta y = 0$) of figure 13. Here, z_{KH} is detected at T_{KH} when $f\phi^+_{u'u'_{ref}} \approx 0.05$. As elaborated previously, it is evident that increasing s^+ (and Re_τ) leads to a discernible reduction in the wall-normal extension of K–H rollers. We speculate that the increasing penetration of relatively large scales into the riblet grooves, with increasing s^+ or Re_τ, affects the velocity mismatch between the valley and above the riblet crest.

6. Summary and conclusions

This study reports a comprehensive experimental investigation into the influence of riblet size on the geometric characteristics of Kelvin–Helmholtz (K–H) rollers, overlying the riblet surfaces. A direct numerical simulations (DNS) database of turbulent channel flow over riblets was utilised initially to develop a novel methodology for identifying these structures based solely on instantaneous streamwise velocity signatures. Our findings revealed that the K–H rollers leave distinct, quasi-periodic signatures in the streamwise velocity component below the riblet crest. Building upon this knowledge, we demonstrated that K–H rollers over riblets could be detected effectively by examining the one-dimensional pre-multiplied spectra of streamwise velocity fluctuations. Additionally, to assess the three-dimensional spatial extent of the rollers, we implemented cross-correlation spectra analysis on two-point streamwise velocity fluctuations acquired in the cross-plane, for varying spanwise and wall-normal offsets.

This study examines the influence of viscous scaled riblet tip spacing (s^+) by employing a well-established experimental approach (e.g. Gatti *et al.* 2020; Endrikat *et al.* 2022; Von Deyn *et al.* 2022) that involves varying the tunnel freestream velocity, which simultaneously affects the friction Reynolds number (Re_τ). Given this methodology, any trends observed in relation to changes in s^+ may also reflect concurrent variations in Re_τ. As these effects are inherently coupled in the current experimental set-up, we have carefully considered this interdependence when interpreting the results, to attribute findings with due caution.

Our investigations using a single normal hot wire traversing the wall-normal plane consistently demonstrated the presence of narrowband frequency structures below the riblet crest (associated with K–H rollers), irrespective of the variation in s^+ (or Re_τ; consider likewise ahead). In particular, the time scale (and consequently the streamwise wavelength) associated with these rollers exhibited a progressive increase with increasing s^+. The cross-spectral analysis between two signals positioned within the same groove, at the same streamwise location, revealed weakening of the K–H rollers with increasing s^+ at the riblet mid-height. This diminishing strength was associated with a reduction in their physical wall-normal extent, with the rollers found to extend across the riblet crest for $s^+ \approx 27$, but becoming confined below the riblet mid-height when $s^+ \approx 110$.

Our investigation also revealed a notable decrease in the physical spanwise extent of the K–H rollers with increasing viscous scaled riblet size. For instance, at $s^+ \approx 43$, the rollers were observed to extend across three riblet grooves along the span, whereas at $s^+ \approx 110$, they were confined to a single groove.

Despite having a matched simulation case for the current experiment at $s^+ \approx 43$ (and $l_g^+ \approx 41$), the analysis of streamwise velocity fluctuations showed that the K–H rollers in the simulation case (RR43) extended over a larger spanwise distance with stronger correlation compared to the experimental case (RR43E). Specifically, the K–H rollers in RR43 extended up to $\Delta y/s \lesssim 10$ (e.g. 10 riblets) or $\Delta y^+ = 430$, while in RR43E, they extended only up to $\Delta y/s \lesssim 2$ (or $\Delta y^+ \approx 90$). We speculate that the difference in K–H roller characteristics between RR43 and RR43E could be attributed to the different Re_τ values: RR43 was simulated in a channel flow at $Re_\tau = 590$, whereas RR43E was conducted in a turbulent boundary layer at $Re_\tau = 1460$. This difference is also evident in the one-dimensional pre-multiplied spectra or co-spectra of streamwise velocity fluctuations, confirming the Re_τ influence on K–H rollers to a certain extent. Although an extensive number of studies on riblets exist in the literature, most focus on the drag reduction regime ($l_g^+ \lesssim 20$), where K–H rollers are weak or only partially developed (Endrikat *et al.* 2021*a*). Even for datasets involving drag-increasing riblets, the formation and characteristics of K–H rollers are rarely discussed, preventing a clear conclusion on their trends at varying Reynolds numbers.

The current findings support that the K–H rollers might not be solely responsible for increasing drag over riblets, as also previously indicated by the simulations of Endrikat *et al.* (2021*a*). It is important to note that the present study follows the same methodology as previous experimental investigations– namely, increasing l_g^+ by increasing Re_τ – and finds that the K–H rollers become statistically insignificant. Further parametric studies are necessary to decouple the effects of s^+ and Re_τ, to determine whether the weakening of K–H rollers is due solely to increasing s^+, Re_τ, or a combination of both, an inquiry that lies beyond the scope of this study. These findings also carry ramifications for the heat transfer enhancing capability of riblets at larger s^+. Prior research (Kuwata 2022; Rouhi *et al.* 2022) has suggested that riblets enhance heat transfer by fostering additional mixing within their grooves, a process facilitated by the presence of K–H rollers. Therefore, the present results underscore the necessity for further investigations to better understand the interplay between riblet size, Reynolds numbers, heat transfer, and the strength and role played by K–H rollers.

Funding. The authors appreciate the financial support of the Australian Research Council (DP200100969 and LP180100712). This research used resources of the Oak Ridge Leadership Computing Facility, which is a DoE Office of Science User Facility supported under Contract DE-AC 05-00OR22725. W.A.R. and R.D. gratefully acknowledge financial support from the University of Melbourne through the Early Career Researcher grant and the Melbourne Postdoctoral Fellowship, respectively.

Declaration of interests. The authors report no conflict of interest.

REFERENCES

ABU ROWIN, W., XIA, Y., WANG, S. & HUTCHINS, N. 2024 Accurately predicting turbulent heat transfer over rough walls: a review of measurement equipment and methods. *Exp. Fluids* **65**, 86.

BAARS, W.J., HUTCHINS, N. & MARUSIC, I. 2017 Self-similarity of wall-attached turbulence in boundary layers. *J. Fluid Mech.* **823**, R2.

BAILEY, S.C.C., HULTMARK, M., SMITS, A.J. & SCHULTZ, M.P. 2008 Azimuthal structure of turbulence in high Reynolds number pipe flow. *J. Fluid Mech.* **615**, 121–138.

BECHERT, D., BRUSE, M., HAGE, W., VAN DER HOEVEN, J. & HOPPE, G. 1997 Experiments on drag-reducing surfaces and their optimization with an adjustable geometry. *J. Fluid Mech.* **338**, 59–87.

BREUGEM, W.P., BOERSMA, B.J. & UITTENBOGAARD, R.E. 2006 The influence of wall permeability on turbulent channel flow. *J. Fluid Mech.* **562**, 35–72.

CHAVARIN, A. & LUHAR, M. 2020 Resolvent analysis for turbulent channel flow with riblets. *AIAA J.* **58** (2), 589–599.

CHAVARIN, A. & LUHAR, M. 2022 Optimization of riblet geometry via the resolvent framework. In *AIAA SCITECH. 2022 Forum*, p. 1037. AIAA.

CHOI, H., MOIN, P. & KIM, J. 1993 Direct numerical simulation of turbulent flow over riblets. *J. Fluid Mech.* **255**, 503–539.

CLAUSER, F. 1954 Turbulent boundary layers in adverse pressure gradients. *J. Aeronaut. Sci.* **21** (2), 91–108.

ALAMO, D., JUAN, C., JIMÉNEZ, J., ZANDONADE, P. & MOSER, R.D. 2004 Scaling of the energy spectra of turbulent channels. *J. Fluid Mech.* **500**, 135–144.

DESHPANDE, R., DE SILVA, C.M., LEE, M., MONTY, J.P. & MARUSIC, I. 2021 Data-driven enhancement of coherent structure-based models for predicting instantaneous wall turbulence. *Intl J. Heat Fluid Flow* **92**, 108879.

DRAZIN, P.G. & REID, W.H. 2004 *Hydrodynamic Stability*. Cambridge University Press.

ENDRIKAT, S., MODESTI, D., GARCÍA-MAYORAL, R., HUTCHINS, N. & CHUNG, D. 2021*a* Influence of riblet shapes on the occurrence of Kelvin–Helmholtz rollers. *J. Fluid Mech.* **913**, A37.

ENDRIKAT, S., MODESTI, D., MACDONALD, M., GARCÍA-MAYORAL, R., HUTCHINS, N. & CHUNG, D. 2021*b* Direct numerical simulations of turbulent flow over various riblet shapes in minimal-span channels. *Flow Turbul. Combust.* **107** (1), 1–29.

ENDRIKAT, S., NEWTON, R., MODESTI, D., GARCÍA-MAYORAL, R., HUTCHINS, N. & CHUNG, D. 2022 Reorganisation of turbulence by large and spanwise-varying riblets. *J. Fluid Mech.* **952**, A27.

FINNIGAN, J. 2000 Turbulence in plant canopies. *Annu. Rev. Fluid Mech.* **32** (1), 519–571.

GARCÍA-MAYORAL, R. & JIMÉNEZ, J. 2011*a* Drag reduction by riblets. *Phil. Trans. R. Soc. A: Math. Phys. Engng Sci.* **369** (1940), 1412–1427.

GARCÍA-MAYORAL, R. & JIMENEZ, J. 2011*b* Hydrodynamic stability and breakdown of the viscous regime over riblets. *J. Fluid Mech.* **678**, 317–347.

GARCÍA-MAYORAL, R. & JIMENEZ, J. 2012 Scaling of turbulent structures in riblet channels up to $Re_\tau \approx 550$. *Phys. Fluids* **24**, 105101.

GATTI, D., VON DEYN, L., FOROOGHI, P. & FROHNAPFEL, B. 2020 Do riblets exhibit fully rough behaviour? *Exp. Fluids* **61** (3), 1–6.

GHISALBERTI, M. & NEPF, H.M. 2002 Mixing layers and coherent structures in vegetated aquatic flows. *J. Geophys. Res. Oceans* **107** (C2), 3–1.

GOLDSTEIN, D.B. & TUAN, T.-C. 1998 Secondary flow induced by riblets. *J. Fluid Mech.* **363**, 115–151.

HAMA, F.R. 1954 Boundary-layer characteristics for smooth and rough surfaces. *Trans. Soc. Nav. Archit. Mar. Engrs* **62**, 333–358.

HO, C.-M. & HUERRE, P. 1984 Perturbed free shear layers. *Annu. Rev. Fluid Mech.* **16** (1), 365–424.

HUTCHINS, N. & MARUSIC, I. 2007 Large-scale influences in near-wall turbulence. *Phil. Trans. R. Soc. A: Math. Phys. Engng Sci.* **365** (1852), 647–664.

HUTCHINS, N., NICKELS, T., MARUSIC, I. & CHONG, M. 2009 Spatial resolution issues in hot-wire anemometry. *J. Fluid Mech.* **635**, 103–136.

JIMÉNEZ, J. 2004 Turbulent flows over rough walls. *Annu. Rev. Fluid Mech.* **36** (1), 173–196.

JIMÉNEZ, J. 2018 Coherent structures in wall-bounded turbulence. *J. Fluid Mech.* **842**, P1.

JIMÉNEZ, J., UHLMANN, M., PINELLI, A. & KAWAHARA, G. 2001 Turbulent shear flow over active and passive porous surfaces. *J. Fluid Mech.* **442**, 89–117.

KHOO, B.C., CHEW, Y.T. & TEO, C.J. 2000 On near-wall hot-wire measurements. *Exp. Fluids* **29** (5), 448–460.

KLINE, S.J., REYNOLDS, W.C., SCHRAUB, F.A. & RUNSTADLER, P.W. 1967 The structure of turbulent boundary layers. *J. Fluid Mech.* **30** (4), 741–773.

KUWATA, Y. 2022 Dissimilar turbulent heat transfer enhancement by Kelvin–Helmholtz rollers over high-aspect-ratio longitudinal ribs. *J. Fluid Mech.* **952**, A21.

LEE, S.-J. & LEE, S.-H. 2001 Flow field analysis of a turbulent boundary layer over a riblet surface. *Exp. Fluids* **30** (2), 153–166.

LIGRANI, P. & BRADSHAW, P. 1987 Spatial resolution and measurement of turbulence in the viscous sublayer using subminiature hot-wire probes. *Exp. Fluids* **5** (6), 407–417.

MONTY, J.P., HARUN, Z. & MARUSIC, I. 2011 A parametric study of adverse pressure gradient turbulent boundary layers. *Intl J. Heat Fluid Flow* **32** (3), 575–585.

MOSER, R.D., KIM, J. & MANSOUR, N. 1999 Direct numerical simulation of turbulent channel flow up to $Re_\tau = 590$. *Phys. Fluids* **11** (4), 943–945.

NEPF, H.M. 2012 Flow and transport in regions with aquatic vegetation. *Annu. Rev. Fluid Mech.* **44** (1), 123–142.

PARK, S.-R. & WALLACE, J.M. 1994 Flow alteration and drag reduction by riblets in a turbulent boundary layer. *AIAA J.* **32** (1), 31–38.

RAMANI, A., SCHILT, L., NUGROHO, B., BUSSE, A., JELLY, T.O., MONTY, J.P. & HUTCHINS, N. 2024 An assessment of effective slope as a parameter for turbulent drag prediction over multi-scaled roughness. *Exp. Fluids* **65** (6), 1–15.

RAN, W., ZARE, A. & JOVANOVIĆ, M.R. 2021 Model-based design of riblets for turbulent drag reduction. *J. Fluid Mech.* **906**, A7.

RAYLEIGH, L. 1880 On the stability, or instability, of certain fluid motions. *Proc. Lond. Math. Soc.* **9**, 57–70.

ROUHI, A., ENDRIKAT, S., MODESTI, D., SANDBERG, R.D., ODA, T., TANIMOTO, K., HUTCHINS, N. & CHUNG, D. 2022 Riblet-generated flow mechanisms that lead to local breaking of Reynolds analogy. *J. Fluid Mech.* **951**, A45.

SANDBERG, R.D. 2015 Compressible-flow DNS with application to airfoil noise. *Flow Turbul. Combust.* **95** (2), 211–229.

SCHLANDERER, S.C., WEYMOUTH, G.D. & SANDBERG, R.D. 2017 The boundary data immersion method for compressible flows with application to aeroacoustics. *J. Comput. Phys.* **333**, 440–461.

SUZUKI, Y. & KASAGI, N. 1994 Turbulent drag reduction mechanism above a riblet surface. *AIAA J.* **32** (9), 1781–1790.

VON, D., LARS, H., GATTI, D. & FROHNAPFEL, B. 2022 From drag-reducing riblets to drag-increasing ridges. *J. Fluid Mech.* **951**, A16.

WALSH, M. 1982 Turbulent boundary layer drag reduction using riblets. In *20th Aerospace Sciences Meeting*, p. 169. AIAA.

WALSH, M. & LINDEMANN, A. 1984 Optimization and application of riblets for turbulent drag reduction. In *22nd Aerospace Sciences Meeting*, p. 347. AIAA.

WALSH, M. & WEINSTEIN, L. 1978 Drag and heat transfer on surfaces with small longitudinal fins. In *11th Fluid and Plasma Dynamics Conference*, p. 1161. AIAA.

WALSH, M.J. 1990 Effect of detailed surface geometry on riblet drag reduction performance. *J. Aircr.* **27** (6), 572–573.